TITLE

Targeted Epigenetic Induction of Mitochondrial Biogenesis Enhances Antitumor Immunity in Mouse Model

AUTHORS

Madhu Malinee[1], Ganesh Namasivayam Pandian[2,*], and Hiroshi Sugiyama[3,4,*]

[1]Department of Anatomy and Developmental Biology, Graduate School of Medicine, Kyoto University, Kyoto, Japan.

[2]Institute of Integrated Cell Material Sciences (iCeMS), Kyoto University of Advanced Study, Kyoto, Japan.

[3]Department of Chemistry, Graduate School of Science, Kyoto University, Kyoto, Japan.

[4]Lead contact

[*]Correspondence: ganesh@kuchem.kyoto-u.ac.jp; hs@kuchem.kyoto-u.ac.jp

SUMMARY

Considering the potential of combinatorial therapies in overcoming existing limitations of cancer immunotherapy, there is an increasing need to identify small-molecule modulators of immune cells capable of augmenting the effect of PD-1 blockade, leading to better cancer treatment. Although epigenetic drugs showed potential in combination therapy, the lack of sequence specificity is a major concern. Here, we identified and developed a DNA-based epigenetic activator with tri-arginine vector called EnPGC-1 that can trigger the targeted induction of the peroxisome proliferator-activated receptor-gamma coactivator 1 alpha/beta (PGC-1α/β), a regulator of mitochondrial biogenesis. EnPGC-1 enhanced mitochondrial activation, energy metabolism, proliferation of $CD8^+$ T cells *in vitro*, and, in particular, enhanced oxidative phosphorylation, a feature of long-lived memory T cells. Genome-wide gene analysis suggested that EnPGC-1 and not the control compounds can regulate T cell activation as a major biological process. EnPGC-1 also synergized with PD-1 blockade to enhance antitumor immunity and improved host survival.

KEYWORDS

Pyrrole-Imidazole Polyamide; Epigenetic activator; PD-1; Cancer Immunotherapy; Mitochondrial biogenesis; Oxidative Phosphorylation

INTRODUCTION

Cancer immunotherapy based on programmed cell death 1 (PD-1)-blockade has gained exponential interest over the last decade because of long-term clinical benefits, and effectiveness over conventional therapies. PD-1 is an immunoinhibitory receptor expressed on activated immune effector $CD8^+$ T cells and regulates tolerance and immunity (Dunn et al., 2004, Fife and Bluestone, 2008). Cancer cells and other immune cells express PD-L1/PD-L2 (ligands of PD-1), and the PD-1/PD-Ls interaction leads to the inactivation of T-cell functions. The blockade of PD-1/PD-Ls axis reinvigorates the T-cell functions and enhances antitumor immunity (Leach et al., 1996, Iwai et al., 2002). The US FDA has approved the PD-1 blockade therapy using mAbs to PD-1 or its ligand PD-L1 for a wide range of cancers (Chamoto et al., 2020, Kumar and Chamoto, 2021).

Despite several advantages of PD-1 blockade therapy, the major limitation is that more than half the population of cancer patients remain unresponsive to PD-1 blockade monotherapy. Although numerous clinical trials have been performed for blocking PD-1/PD-Ls alone or in combination with other negative receptors (such as Lag3 and Tim-3) or other physicochemical therapies, the clinical outcomes reported to date are not satisfactory. Consequently, efforts are on developing novel cost-effective combination therapies aimed at rescuing the less-responsive cancer patients.

Mitochondrial activation is known to be critical for $CD8^+$ T-cell activation, proliferation, and memory cell fate determination during immune responses (Weinberg et al., 2015, Buck et al., 2016, Buck et al., 2017, van der Windt et al., 2013, Sena et al., 2013). Recently, Honjo group demonstrated that mitochondrial-activating chemicals improve PD-1 blockade (Chamoto et al., 2017) and revealed that reactive oxygen species (ROS) generators (e.g., DNP, Luperox) and mitochondrial uncouplers (e.g., FCCP) could synergize the tumoricidal effect of PD-1 blockade where the cytotoxic T lymphocytes (CTLs) showed enhanced AMPK and mTOR expression in the combination group. Further, they found PGC-1α (the downstream molecule of AMPK/mTOR) upregulated in the combination group and a series of chemical activators of this 'ROS-AMPK/mTOR-PGC-1' pathway synergize with PD-1 blockade and enhances antitumor immunity (Chamoto et al., 2017). PGC-1α, and PGC-1β, the known coactivators, form complexes with different transcription factors (TFs) and regulate the expression of genes associated with mitochondrial biogenesis, metabolism, oxidative phosphorylation (OXPHOS), fatty acid oxidation (FAO), and mitochondrial cristae reorganization (Lin et al., 2005, St-Pierre et al., 2003). Based on these reports, enhancing mitochondrial OXPHOS and FAO in $CD8^+$ T cells could be a good approach to boost antitumor immunity in combination with PD-1 blockade therapy.

Small-molecule modulators of epigenetic enzymes have shown clinical potential to enhance the efficacy of cancer immunotherapy owing to their potency to alter multi-gene networks (Zhu et al., 2016, Gallagher et al., 2017). However, the lack of sequence selectivity leading to potential side effects and toxicity has been a major road barrier in their clinical use. Therefore, artificial transcriptional control achieved by combining the epigenetic modulator with a sequence-recognizing ligand is in demand (Zhu et al., 2016, Kobayashi et al., 2021). The Dervan group first developed the small-molecular compound pyrrole–imidazole polyamide (PIP), which can recognize DNA base pairs with sequence specificity (Dervan and Edelson, 2003). An antiparallel pairing of imidazole and pyrrole (I–P) recognizes a G:C base pair, whereas a pyrrole-pyrrole pairing (P–P) recognizes A:T or T:A. The unique properties of PIP molecules, e.g., sequence specificity, smooth permeability to the cell/nuclear membrane, and binding affinity similar to that of natural TFs, render it a promising small-molecule candidate for therapeutic usage (Takahashi et al., 2008, Hiraoka et al., 2015, Malinee et al., 2020). We harnessed the capability of sequence-specific binding of PIPs and supplemented selectivity to epigenetic modulators (e.g., SAHA (Suberoylanilide hydroxamic acid), a histone deacetylase (HDAC) inhibitor and an epigenetic eraser; and CTB (N-(4-chloro-3-trifluoromethyl-phenyl)-2-ethoxy-benzamide), a histone acetyl transferase (HAT) activator and an epigenetic writer) by conjugating them with PIPs (Pandian et al., 2014b, Han et al., 2015, Pandian et al., 2014a).

Here, we show the identification and development of a designer ligand conjugated with bromodomain inhibitor (BI), an epigenetic reader capable of inducing the expression of PGC-1α/β and termed it as EnPGC-1. EnPGC-1 remarkably activated the downstream genes of PGC-1α/β that regulate OXPHOS, FAO, and longevity of $CD8^+$ T cells both *in vitro* and *in vivo*. Furthermore, the combination therapy using EnPGC-1 with PD-1 blockade notably enhanced antitumor immunity and improved the survival of tumor-bearing mice compared with PD-1 blockade or PIP alone treatment. Our programmable DNA-based epigenetic activator could open a new avenue to treat less-responsive cancer patients in combination with PD-1 blockade.

RESULTS

Design of epigenetically active PIP (EnPGC-1) for PGC-1α/β activation

Considering the clinical importance of modulating PGC-1 expression, we screened our databank generated from a library of SAHA-conjugated PIPs on human dermal fibroblast (HDF) cells for a specific PIP sequence that upregulates the mitochondrial-biogenesis-associated gene network. While analyzing the microarray results of a library of 32 SAHA-PIPs (Pandian et al., 2014b), we discovered a PIP named SAHA-PIP 'R' that specifically activated the endogenous expression of PGC-1α (encoded by PPARGC1A gene) and PGC-1β (encoded by PPARGC1B gene) in HDF cells (Figure S1A). This preliminary finding suggests that the PIP sequence R may have the specificity toward gene PPARGC1A/B (Figure S1B, S6). We verified the microarray data by treating HDF cells with SAHA-R for 48 h and quantified the transcript level of PGC-1α/β (Figure S1 C-D). We also confirmed the target specificity of the sequence R toward the activation of PGC-1α/β using HAT activator (CTB)-conjugated PIP R (Figure S1D). However, the epigenetic modifiers SAHA and CTB are indirect approach to gene activation that solely depend on the presence of the HAT enzyme in the gene vicinity. To improve gene activation, we hypothesized that the recruitment of epigenetic activators for histone acetylation could be a more direct and improved way to activate a gene of interest compared with the blockage of the epigenetic suppressor. Recently, our research group developed a novel epigenetic modulator for locus-specific acetylation that can directly recruit the acetylation machinery (P300/CBP) in the PIP-binding region. This epigenetic reader (bromodomain inhibitor, BI) recognizes the bromodomain (BD) of the p300 protein (Taniguchi et al., 2018). Furthermore, the HAT domain of p300 facilitates sequence-specific acetylation in the PIP-binding region. To harness the benefit of this strategy, we conjugated PIP sequence R with BI and tested the effect of BI-R on HDF cells (Figure S1B). Compared with SAHA-R and CTB-R, BI-R yields a better enhancement in the expression of PGC-1α as well as PGC-1β (Figure S1 C-D). Notably, the control molecules 'R

alone' and 'BI alone' did not enhance the PGC-1α/β transcript levels, as per our expectation, because BI alone does not have sequence specificity, and R alone, although it has sequence specificity, but it lacks functional epigenetic activity; however, their combination (i.e., BI-R) had both sequence specificity as well as functional epigenetic activity (Figure S1D). This implies that specifically, cognate sequence of R is directly or indirectly involved in the upregulation of PGC-1α/β.

In further development, we added three arginine repeats at the C-terminal of BI-R, which eases the uptake of PIPs in the cell (Hidaka et al., 2020). We named this designer ligand Bi-R-Arg3 (BI-R with three arginine repeats) as EnPGC-1. The structure of EnPGC-1 is shown in Figure 1A. The expression of PGC-1α/β at the transcript level was enhanced in HDF cells treated with EnPGC-1 in a dose-dependent manner compared with the DMSO vehicle treatment (Figure S1E).

Recent work suggests that enhancing OXPHOS in $CD8^+$ T cells boosts the longevity of T cells and improves antitumor immunity (Chamoto et al., 2017) and the effector T cells are known to become less active in the suppressive tumor microenvironment because of reduced PGC-1 expression (Scharping et al., 2016). PGC-1α and PGC-1β possess homology and have a similar gene regulation pattern (Lin et al., 2002, Kressler et al., 2002). Since these coactivators share common structural features in the protein structure in human and mice, we were curious to examine whether EnPGC-1 could enhance PGC-1α/β expression in mouse primary $CD8^+$ T cells *in vitro*. Following the schedule mentioned in Figure 1B, we quantified the transcript level of PGC-1α/β in $CD8^+$ T cells and found that EnPGC-1 affords a better enhancement of the expression of PGC-1α and PGC-1β compared with BI-R (Figure 1C). Further, the transcript levels of PGC-1α/β were enhanced significantly ($p<0.05$) in a dose-dependent manner by EnPGC-1 treatment compared with DMSO and control conjugated mismatch PIP (BI-Ctrl-Arg3, Control PIP hereafter) (Figure 1D). 'Control PIP' has a similar chemical architecture to EnPGC-1 but has different sequence recognition (Figure S1F, S6). Further, we quantified the expression of PGC-1α/β at the protein level by staining intranuclearly in treated $CD8^+$ T cells using flow cytometry. EnPGC-1 notably enhanced the expression of PGC-1α/β while the control PIPs did not (Figure 1E).

Together, these results suggest that EnPGC-1 enhances the expression of PGC-1α/β while the control PIP with similar architecture but different sequence recognition does not show PGC-1α/β enhancement. Notably, EnPGC-1 (arginine-conjugated BI-R) yields improved enhancement in the expression of PGC-1α/β compared with other epigenetic activator conjugated PIP (e.g., SAHA-R/CTB-R) and BI-R. The control BI alone and PIP R alone that lacks sequence specificity and epigenetic activity, respectively, have no effect.

We hypothesize that EnPGC-1, a bifunctional molecule, functions via binding to p300's

bromodomain and recruiting it to PIP-binding region that causes acetylation and gene expression. To test our hypothesis, we performed squelching assay where we used SGC-CBP30, a potent CREBBP/EP300 (CBP/p300) inhibitor to test whether co-administration of free SGC-CBP30 cancels the gene enhancement effect of EnPGC-1. We treated murine primary $CD8^+$ T cells following the schedule mentioned in Figure 1B. We found that the co-administration of SGC-CBP30 significantly ($p < 0.05$) reduces the gene expression level of PGC-1α/β compared to EnPGC-1 alone (Figure 1F and S1G). Further, we tested the involvement of acetyltransferase activity of p300 for EnPGC-1 mediated gene induction. We co-administered A-485, a potent p300 acetyltransferase inhibitor to $CD8^+$ T cell culture along with EnPGC-1. The co-administration of A-485 abrogates the effect of EnPGC-1. The co-administration of A-485 significantly ($p < 0.001$) reduces the gene expression level compared to treatment with EnPGC-1 alone which further strengthen the mechanism of action of bifunctional EnPGC-1 for enhancing the PGC-1 gene expression (Figure 1G and S1H). Together, these two results suggest that EnPGC-1 function as a bifunctional recruiter and induces HAT activity of p300.

EnPGC-1 enhances mitochondrial function and proliferation in murine $CD8^+$ T cells in vitro

As PGC-1 is the master regulator of mitochondrial activation and biogenesis, we assessed mitochondrial activation parameters in murine primary $CD8^+$ T cells treated with EnPGC-1 as per the schedule in Figure 1B. We found that EnPGC-1 and not Control PIP enhanced mitochondrial activation parameters (mitochondrial mass, potential, mitochondrial superoxide (MSOX), and cellular ROS (CROX)) in $CD8^+$ T cells (Figure 2A). Further, using Seahorse flux analyzer, we measured both mitochondrial respiration (denoted by the oxygen consumption rate, OCR) and glycolytic respiration (denoted by the extracellular acidification rate, ECAR) (Figure S2A). EnPGC-1 treatment shows enhancement in OCR dose-dependently in $CD8^+$ T cells (Figure 2B, upper panel). Further, OCR-associated parameters, such as basal respiration, maximal respiration, and ATP turnover were higher in the EnPGC-1-treated condition over DMSO vehicle, while the controls e.g., BI alone and R alone did not show any enhancement (Figure 2B, lower panel). Notably, spare respiratory capacity (SRC) which is linked to cell survival, was significantly ($p<0.01$) higher in the EnPGC-1 treated group over DMSO vehicle and other controls (Figure 2B, lower panel). Enhancement of SRC by EnPGC-1 treatment suggests that $CD8^+$ T cells can survive longer (van der Windt et al., 2012). A similar enhancement in OCR was observed dose-dependently in HDF cells (Figure S2B).

It is reported that cardiomyocytes express both PGC-1α and PGC-1β (Lin et al., 2002, Puigserver et al., 1998); thus, we tested the effect of EnPGC-1 and measured the OCR, which

we confirmed enhanced compared with the DMSO vehicle treatment (Figure S2C).

Besides, we measured glycolytic respiration and found that EnPGC-1 treatment enhanced it minimally in $CD8^+$ T cells (Figure S2D). Furthermore, we calculated the ratio of basal OCR/basal ECAR in treated $CD8^+$ T cells suggesting the selective dependency of cells regarding their energy demand (Figure 2C). The higher OCR/ECAR value observed in the EnPGC-1-treated condition suggests that EnPGC-1 treatment skews the $CD8^+$ T cell metabolism toward more OXPHOS (Figure 2C). Increased mitochondrial activation parameters and OCR together indicate that the induced expression of PGC-1α/β by EnPGC-1 treatment results in skewed metabolism toward OXPHOS.

TCR stimulation in naïve $CD8^+$ T cells triggers a plethora of signaling networks. During priming, T cells depend primarily upon glycolysis for their bioenergetic needs and anabolic profile (van der Windt and Pearce, 2012, Pearce, 2010). We tested whether the enforced PGC-1α/β expression and mitochondrial enhancement during TCR stimulation have any positive effect on the early phase of $CD8^+$ T cell differentiation and proliferation; we assessed the proliferation of $CD8^+$ T cells using the dye dilution method and compared the rate of proliferation among the treated groups. The frequency of daughter populations was plotted in a stacked graph (Figure 2D). Interestingly, we found that EnPGC-1 treatment enhanced the proliferation of $CD8^+$ T cells in a dose-dependent manner (Figure 2D). Proliferation assessment using Ki67 (a proliferation marker) gives a similar result (Figure 2E). Based on this result, we conclude that enhancing mitochondrial activation by EnPGC-1 treatment positively regulates T cells differentiation at the early phase.

The coactivators PGC-1α/β are inducers of mitochondrial biogenesis and respiration and they modulate the composition and function of individual mitochondria (Lin et al., 2002). Curiously, we assessed mitochondrial DNA (mtDNA) copy number (mt-ND1/nu-HK2). The result suggests that EnPGC-1-induced PGC-1α/β upregulation increased mtDNA copy number suggestive of enhanced mitochondrial biogenesis in $CD8^+$ T cells (Figure 2F).

PGC-1α/β is a known transcriptional coactivator that controls global oxidative metabolism (OXPHOS, FAO) by establishing complexes with TFs e.g., PPAR, NRF, and ERR (Villena and Kralli, 2008). Acyl-CoA dehydrogenase long chain (LCAD), and acyl-CoA dehydrogenase medium chain (MCAD) are important enzymes associated with FAO, which were found upregulated in the EnPGC-1-treated group (Figure 2G). Since EnPGC-1 treatment enhances OXPHOS, we quantified transcript level of ATP synthase F1 subunit alpha (ATP5a1), a subunit of ATP synthase enzyme which catalyzes ATP synthesis using an electrochemical gradient of protons across the inner membrane during OXPHOS. The transcript level of ATP5a1 was higher in EnPGC-1 treated group over DMSO-treated (Figure 2G). The expression level of ATP5a1 is in line with our phenotypic observation (enhanced

OCR) (Figure 2B).

Since enhanced OXPHOS and FAO improves the longevity of cells, we quantified the transcript level of anti-apoptotic genes Bcl2 and Birc3 in the *in vitro* stimulated $CD8^+$ T cells treated with EnPGC-1 (van der Windt et al., 2012, Chowdhury et al., 2018). EnPGC-1 treated $CD8^+$ T cells show higher expression level of Bcl2 and Birc3 (Figure 2H).

Taken together, EnPGC-1 contributed to an increase in oxidative metabolism by enhancing mitochondrial respiration (OXPHOS and FAO), and mitochondrial biogenesis (mtDNA copy number). Importantly, this elevated oxidative metabolism by EnPGC-1 results in enhanced T cell differentiation to effector population at an early phase with enhanced longevity.

EnPGC-1 triggers sequence-specific activation of PGC-1 α/β expression through targeted acetylation

To address the specificity of EnPGC-1 for the activation of PGC-1α/β expression, we used a siRNA-mediated knockdown assay to test whether EnPGC-1 can rescue the gene expression. We transfected naïve $CD8^+$ T cells with a siRNA against the transcript of PGC-1α and treated with or without EnPGC-1 along with TCR stimulation (Figure 3A). Treatment with the siRNA against PGC-1α reduced the level of PGC-1α transcript ($p = 0.0047$). The enhanced expression of PGC-1α by EnPGC-1 treatment rescued the effect of siRNA when administered together with the siRNA (Figure 3B). A similar result was obtained for the siRNA-mediated knockdown of PGC-1β expression, suggesting the direct effect of EnPGC-1 in the activation of PGC-1α and PGC-1β at the transcript level (Figure 3B; Figure S3A). Furthermore, the controls (BI alone, R alone and control PIP) did not rescue the siRNA effect (Figure 3B-C).

To examine the binding affinity and sequence selectivity of EnPGC-1, a DNA melting temperature (*T*m) assay was performed (Vaijayanthi et al., 2012). *T*m assay allows the measurement of relative binding affinities through the *T*m and Δ *T*m values (Δ *T*m = *T*m (DNA + PIP) − *T*m (DNA)). To confirm the binding, dsDNA templates were prepared, e.g., a matched DNA template (5'-GGCACGCCTCGG-3' (EnPGC1-DNA), and a mismatched DNA template with a different sequence (5'-GGCAGACGTCGG-3' (Mismatch-DNA)); the binding sites are underlined. The result of *T*m assay confirmed the binding of EnPGC-1 to the target DNA as a *T*m shift of 19.99 ◦C was observed, while the *T*m shift was only 1.85 ◦C for mismatch control DNA (Figure S3B). The low Δ *T*m shift recorded for the mismatch DNA in the presence of EnPGC-1 indicates a lower affinity of EnPGC-1 for sequences other than the target DNA.

Histone acetylation is a primary transcription activation marker for opening up the chromatin and 'Switching ON' the gene expression (Turner, 1991, Verdone et al., 2006). Based on the design of bifunctional compound EnPGC-1, in which the `Bi` component is

meant to recruit the acetylation machinery of p300/CBP, we performed chromatin immunoprecipitation (ChIP) assay of p300 in murine $CD8^+$ T cells treated with EnPGC-1 for 48 h. A sequence of ~ 200 bp from the transcription start site (TSS) in Ppgargc1a and Ppargc1b promoter region were used to test the enrichment of p300 binding. As shown in Figure 3D, a significant ($p < 0.05$) enrichment of p300 binding in the promoter region of both PGC-1α and PGC-1β was observed. A similar result was obtained for B16 (murine melanoma) cells where p300 and H4-pan acetylation are significantly ($p < 0.05$) enriched in EnPGC-1 treated group than DMSO vehicle or control BI and R (Figure S3C-E).

Furthermore, we examined the genome-wide H3K27Ac acetylation induced by EnPGC-1 in murine $CD8^+$ T cells. The qPCR of H3K27Ac-ChIP suggested a significant ($p < 0.05$) enrichment in the promoter region of both PGC-1α and PGC-1β (Figure 3D). ChIP-sequencing analysis revealed a notable peak enrichment near TSS in the promoter region of PGC-1α and PGC-1β in $CD8^+$ T cells treated with EnPGC-1 over DMSO vehicle (GEO accession number GSE175849) (Figure 3E). It is important to note here that two potential binding sites of EnPGC-1 was observed in the promoter region of PGC-1α/β where H3K27 was significantly enriched (Figure S4A).

We then performed RNA-Sequencing (RNA-Seq) to verify if EnPGC-1 induces unique gene expression profile compared to SGC-CBP30 and control PIP (having similar chemical architecture but different recognition site) (GEO accession number GSE174750). RNA-Seq analysis of *in vitro* treated murine primary $CD8^+$ T cells revealed that 2308 genes (p-value < 0.05) were differentially expressed in EnPGC-1 treated cells over DMSO where 871 genes were upregulated, and 1437 genes were downregulated (Figure S4B).

Gene ontology (GO) analysis with differentially expressed genes (p-value < 0.05) suggested that EnPGC-1 can activate immune response associated pathways as the major biological processes that included T cell activation, lymphocyte proliferation, IFN-γ signaling, and leucocyte cell-cell adhesion (Figure 3F (left panal), Table S2). On the other hand, SGC-CBP30-treated cells did not show the immune response associated pathways rather show an entirely different set of genes (Figure 3F, right panel). The biological processes in the Control PIP-treated cells were unrelated to immune response associated pathways that further verified the site-specific gene activation in the genome-wide gene level (Figure 3G and S4C).

A heatmap of EnPGC-1-activated genes plotted along with the controls showed that the genes associated with T cell activation and maturation (Dpp4 and Tcf7) (Shao et al., 2020) and IFN-γ signaling process (Stat1, Jak2, and Gbp7/8) (Schroder et al., 2004) were notably activated by EnPGC-1 when compared to that with controls (Figure 3G). PGC-1α signaling modulates T-cell differentiation through fatty acid and OXPHOS metabolism (Choi and Bothwell, 2012). RNA-Seq analysis showed that EnPGC-1 upregulated PGC-1α (by 3.6-fold).

Further, the genes related to fatty acid metabolism like Slc12a7 (fatty acid transporter) and Cpt1a (a rate-limiting enzyme for FAO) were enhanced, which suggests that EnPGC-1 mediates FAO. Importantly, Aldoa, a gene involved in glucose metabolism is decreased in EnPGC-1 treated cells. Also, the genes associated with the electron transport chain (OXPHOS) (e.g., Atp10d, Atp1b2) were upregulated in EnPGC-1 treated cells (Figure 3G). The enhanced transcript level of Lcad, Mcad, and Atp5a1 in the *in vitro* stimulated and EnPGC-1 treated $CD8^+$ T cells as shown in Figure 2G further supports that EnPGC-1 could enhance OXPHOS and FAO. Together, our results support the hypothesis that EnPGC-1 mediated induction of PGC-1 skews the metabolism towards OXPHOS/FAO.

EnPGC-1 in combination with PD-1 blockade enhances antitumor immunity

Encouraged by our *in vitro* findings that EnPGC-1 enhances PGC-1α/β-mediated mitochondrial metabolism, OXPHOS, FAO, and longevity in murine $CD8^+$ T cells, we wondered whether EnPGC-1 could improve the effect of PD-1 blockade and enhances the antitumor immunity *in vivo*. To test our hypothesis, we performed a combination therapy on MC38 (colon adenocarcinoma; responsive tumor, (Juneja et al., 2017)) tumor-bearing mice using EnPGC-1 (1 mg/kg) and PD-1 blockade (using anti-PD-L1 mAb) (Figure 4A) (Kumar et al., 2020). EnPGC-1 in combination with PD-1 blockade yielded better tumor regression as well as improved survival compared with PD-1 blockade alone (Figure 4B, C). EnPGC-1 alone or the control molecules BI and R alone have no tumor regression effect and were not able to enhance the survival of tumor-bearing host (Figure 4B, C). The *in vivo* result indicates EnPGC-1 synergizes with PD-1 blockade therapy and enhances antitumor immunity.

Further, to understand how EnPGC-1 and PD-1 blockade combination ameliorates the antitumor immunity, we analyzed the experimental groups one day after the third treatment of EnPGC-1 *in vivo* following the schedule shown in Figure 4A. $CD8^+$ T cells from draining lymph nodes (DLN) and tumor mass were analyzed. The absolute number of DLN cells (total DLN cells per DLN) was higher in the combination group compared with anti-PD-L1 mAb alone (Figure 4D). Since the effector memory ($CD62L^{low}$ $CD44^{high}$) $CD8^+$ T cells in DLN are destined to leave to the periphery and infiltrate the tumor mass, we compared the effector memory population among different groups and found that the frequency and the absolute number of effector memory cells were increased in EnPGC-1 combination group significantly ($p<0.05$) compared with PD-1 blockade alone (Figure 4E).

As $CD8^+$ TILs are the real effectors to kill tumor cells and the higher frequency of infiltrated $CD8^+$ T cells is the prognostic marker of immune responses, we assessed $CD8^+$ TILs in the tumor mass (Idos et al., 2020). The result suggests that the frequency of infiltrated $CD8^+$ T lymphocytes was higher in the combination group (Figure 4F and S5A). Further, $CD8^+$ TILs

from the EnPGC-1 combination group show higher mitochondrial potential, mSOX, and cellular ROS than Ctrl IgG- and anti-PD-L1 mAb alone treated group (Figure 4G). Similar mitochondrial activation was observed in DLN $CD8^+$ T cells in EnPGC-1 combination group (Figure S5B). In addition, we measured OCR to assess OXPHOS in $CD8^+$ T cells (purified from pooled DLN cells). The EnPGC-1 combination exhibited significantly ($p<0.05$) higher OCR values and its associated parameters than PD-1 blockade alone (Figure 4H). Interestingly, SRC was remarkably enhanced in combination treatment that could result in improved longevity of effector population *in vivo* (Figure 4H). This result is in line with our *in vitro* finding where EnPGC-1 enhances SRC of $CD8^+$ T cells (Figure 2B). We also measured glycolytic respiration of DLN $CD8^+$ T cells (Figure S5C). Since PD-1 blockade augments the proliferation of short-lived effector $CD8^+$ T cells with glycolytic respiration, the less availability of effector T cells because of apoptotic death could be one of the possible reasons for less responsiveness in some patients (Patsoukis et al., 2015). To understand the dependency of T cells on OXPHOS/glycolysis, we plotted OCR/ECAR values and observed slightly higher glycolytic respiration (shown by ECAR) under PD-1 blockade alone condition (Figure 4I). The combination of PD-1 blockade with EnPGC-1 (PGC-1α/β activator) shifts the T cell dependency towards more OXPHOS than ECAR for the energy demand. This suggests skewing T cell energy metabolism towards OXPHOS enhances the effect of PD-1 blockade which we observed in combination group. Our result is consistent with other research groups where they have shown the drugs that enhance mitochondrial respiration improve PD-1 blockade effect (Chowdhury et al., 2018, Wan et al., 2020).

To assess the effector function, we quantified IFN- γ intracellularly in $CD8^+$ TILs. The IFN-γ^+ $CD8^+$ TILs were higher in frequency in the combination group than PD-1 blockade alone (Figure 4J).

PGC-1 family coactivators upregulate the OXPHOS and FAO metabolism (Villena and Kralli, 2008). We curiously measured the FAO in DLN $CD8^+$ T cells from *in vivo* experimental animals. $CD8^+$ T cells from the combination group showed higher expression of FAO compared to PD-1 blockade alone or Ctrl IgG treatment (Figure 4K). Induction of FAO in combination group again supports the improved life of effector T cells in combating the tumor cells and enhancing antitumor immunity (Chowdhury et al., 2018, Wan et al., 2020). We further quantified the transcript level of genes associated with FAO in the purified DLN $CD8^+$ T cells from *in vivo* treated groups (one day after 3rd treatment of EnPGC-1) and found higher transcript levels of MCAD and Cpt1a in the combination group compared to PD-1 blockade alone (Figure 4L). Further, the transcript level of PGC-1α/β, Uqcrc1, Nrf2 were also increased in the combination group (Figure 4L). The enhanced OXPHOS, FAO in the combination group improves the longevity of T cells as indicated by elevated transcript level

of Bcl2 (Figure 4L) (Paumen et al., 1997). Genes associated with mitochondrial biogenesis like Mitofusin 1 (Mfn1, mediates mitochondrial clustering) and mitochondrial transcription factor A (TFAM, play a role in organizing and compacting mitochondrial DNA) have shown a trend of increment in combination compared to PD-1 blockade alone (Figure S5D) (Picca and Lezza, 2015).

To conclude, the compound EnPGC-1 upregulated OXPHOS and FAO in $CD8^+$ T cells, which improves the longevity and effector functions of killer T cells and augments the efficacy of PD-1 blockade in combination.

DISCUSSION

Though PD-1 blockade therapy surpassed the standard methods of cancer treatment (Topalian et al., 2015, Couzin-Frankel, 2013), unresponsiveness in a significant fraction of patients is the major limitation that needs attention (Zou et al., 2016). The paucity of effector cells (because PD-1 blockade induced vigorously glycolysis performing effector T cells undergo apoptotic death (Patsoukis et al., 2015)) at tumor sites could be one of the reasons for the unresponsiveness observed in some patients (Azimi et al., 2012, Mahmoud et al., 2011). Other research groups have emphasized the importance of inducing OXPHOS and FAO for enhancing antitumor immunity, as they generate long-lived T cells (Chowdhury et al., 2018).

In the current work, we skewed the $CD8^+$ T-cell metabolism toward OXPHOS and FAO by upregulating PGC-1α and PGC-1β, using a dual-functional molecule, EnPGC-1, encompassing the P300/CBP-selective bromodomain inhibitor which acts as a P300/CBP recruiter. Further, EnPGC-1 mediated PGC-1α/β upregulation enhanced antitumor immunity *via* increased tumor-infiltrating $CD8^+$ T cell frequency with enhanced mitochondrial function, OXPHOS/FAO metabolism, effector functions and Bcl2 level *in vivo*. FAO is known for memory-like cell generation with enhanced Bcl2 level (Pearce et al., 2009, Paumen et al., 1997, Perianayagam et al., 2006). SRC enhancement in CTLs by EnPGC-1 mediated PGC-1α/β upregulation suggests that CTLs can survive longer and increase their number in a memory-like pool (van der Windt et al., 2012, van der Windt and Pearce, 2012).

EnPGC-1 is expected to have a negligible effect on tumor cells and non-toxic owing to their lower doses (*in vivo* dose 1mg/kg, equivalent to 3.87 μM) used in this study (Figure S5E) as evident by similar tumor growth and survival of Ctrl IgG and EnPGC-1 treated group (Figure 4B-C). Furthermore, tumor cells are less sensitive to EnPGC-1 for enhancing OCR at physiological ranges (Figure S5F).

The programmable nature of EnPGC-1 allows them to alter their chemical architecture and improve their bioefficacy. Here, we chose CBP30 as the functional ligand of EnPGC-1 owing to their synthetic accessibility of building blocks. While EnPGC-1 demonstrated notable

bioactivity, they have limited selectivity over BET bromodomains. Therefore, more specific inhibitors with higher selectivity over BET bromodomains could further enhance bioefficacy. Through the data generated by independent lines of evidence, we suggested the recruitment of p300 acetyltransferase as the mechanism behind EnPGC-1-mediated gene activation. Dancy et. al., showed the essential role of the p300/CBP bromodomain for the catalytic activity of their acetyl transferase domain (Zucconi et al., 2016, Dancy et al., 2012). Further studies are warranted to gain deeper insights into whether the modulation of the coactivator binding site interface could indirectly affect EnPGC-1-mediated gene expression. According to our previous report, our epigenetic activator operates through site-specific transcription activation. As shown in Figure 3E, the genome-wide acetylation profile showed a prominent enrichment of H3K27 acetylation in the promoter region of both PGC-1α and PGC-1β in $CD8^+$ T cells treated with EnPGC-1 and not with DMSO. To clarify, if EnPGC-1 have binding sites in the promoter, we performed sequence alignment of the promoter sequences in human and mouse and observed 65% homology in PGC-1α, and 63% sequence homology in PGC-1β. While there are potential binding sites in the notably acetylated region of PGC-1α and PGC-1β in EnPGC-1 treated cells (Figure S4A), it is not straightforward to verify the exact homologous sequence targetable by PIP as EnPGC-1 recognizes only six base pairs and can have cognate binding sites across the entire genome. However, the genome-wide transcriptome analysis showed that the major biological process of EnPGC-1 upregulated genes corresponds to T cell activation (Dpp4 and Tcf7), OXPHOS (Atp10d, Atp1b2), lipid metabolism (Slc12a7 and Cpt1a), and regulation of leucocyte cell to cell adhesion in the EnPGC-1 treated cells. Future studies to advance EnPGC-1 for clinical application need rational design considering the points mentioned and delivering them specifically to T cells by incorporating aptamers and short peptides to reduce their off-target effects (Bai et al., 2020). Because PGC-1 signaling is known to be essential for energy metabolism (Lin et al., 2005, St-Pierre et al., 2003), EnPGC-1 can potentially be developed as a drug not just for enhancing antitumor immunity but also for hyperlipidemia and type 2 diabetes. Although the pharmacokinetics of different versions of PIPs were studied before (Synold et al., 2012, Fukasawa et al., 2009), the pharmacokinetic properties of EnPGC-1 need to be tested to validate their clinical prospects.

Nevertheless, we have shown that the EnPGC-1-mediated induction of PGC-1α/β enhances mitochondrial biogenesis and global oxidative metabolism. Our proof-of-concept study substantiates the potential of DNA-based programmable small molecules to control the key regulatory factors associated with T-cell-based immune responses against cancer. PIPs have the potential to be developed to meet the unmet needs in cancer immunotherapy because of their special features such as their small size, binding to a DNA sequence with an affinity

similar to that of a transcription factor, permeability to the cell membrane, cost-effectiveness, solid-phase synthesis, and low or no immunogenicity.

SIGNIFICANCE

Despite the wide success of PD-1 blockade therapy, still a significant fraction of cancer patients do not respond to PD-1 blockade-based monotherapy. Unresponsiveness could be attributed to a) insufficient number of effector cells due to apoptosis and b) reduced PGC-1 expression in effector T cells in the suppressive tumor microenvironment. While epigenetic drugs have shown potential in cancer treatment, lack of programmable nature and sequence selectivity has been major road barrier in their clinical use. In this work, we harnessed the selective DNA-binding capability of pyrrole–imidazole polyamides and guided an epigenetic reader to enable targeted epigenetic induction of PGC-1 that regulates mitochondrial biogenesis in $CD8^+$ T cells. The epigenetic reader, EnPGC-1 enhances the mitochondrial activation, proliferation, and OXPHOS in $CD8^+$ T cells *in vitro*. Furthermore, EnPGC-1 synergizes with PD-1 blockade therapy *in vivo* and enhances the number of tumor-infiltrating $CD8^+$ T cells and skewed their metabolism towards OXPHOS/FAO with memory-like cells having enhanced longevity. Together, this study represents the first example of a programmable DNA-based epigenetic drug that could open a new avenue to treat less-responsive cancer patients in combination with PD-1 blockade cancer immunotherapy. Since EnPGC-1 enhances PGC-1α/β, it may be fine-tuned for treating hyperlipidemia, type 2 diabetes, and OXPHOS-related mitochondrial disorders.

ACKOWLEDGMENTS

We thank Hashiya Kaori, Shuji Ikeda, and Shinsuke Sato for PIP synthesis; Kandarp Joshi for performing the RNA-Sequencing analysis and data visualization; 'medical support center' for providing Seahorse flux analyzer facility; 'iCeMS support center, Kyoto University' for flow cytometry equipment to assist us. We express sincere thanks for a Grant-in-Aid Priority Research (16H06356 to H. S.) and 20H05936 from JSPS. This work was also supported by AMED [JP20am0101101 to H. S. (Platform Project for Supporting Drug Discovery and Life Science Research (BINDS) and NIH award R01CA236350 to H. S.

AUTHOR CONTRIBUTION

Conceptualization, G.N.P., and H.S.; Methodology, M.M.; Organic synthesis, M.M.; *in vitro* cell assays and *in vivo* experiment, M.M.; Analysis and interpretation of data, M.M.; Writing – Original Draft, M.M.; Writing – Review & Editing, G.N.P, and H.S.; Supervision, G.N.P. and H.S.

DECLARATION OF INTETERESTS

The authors declare no competing interests.

Figure 1

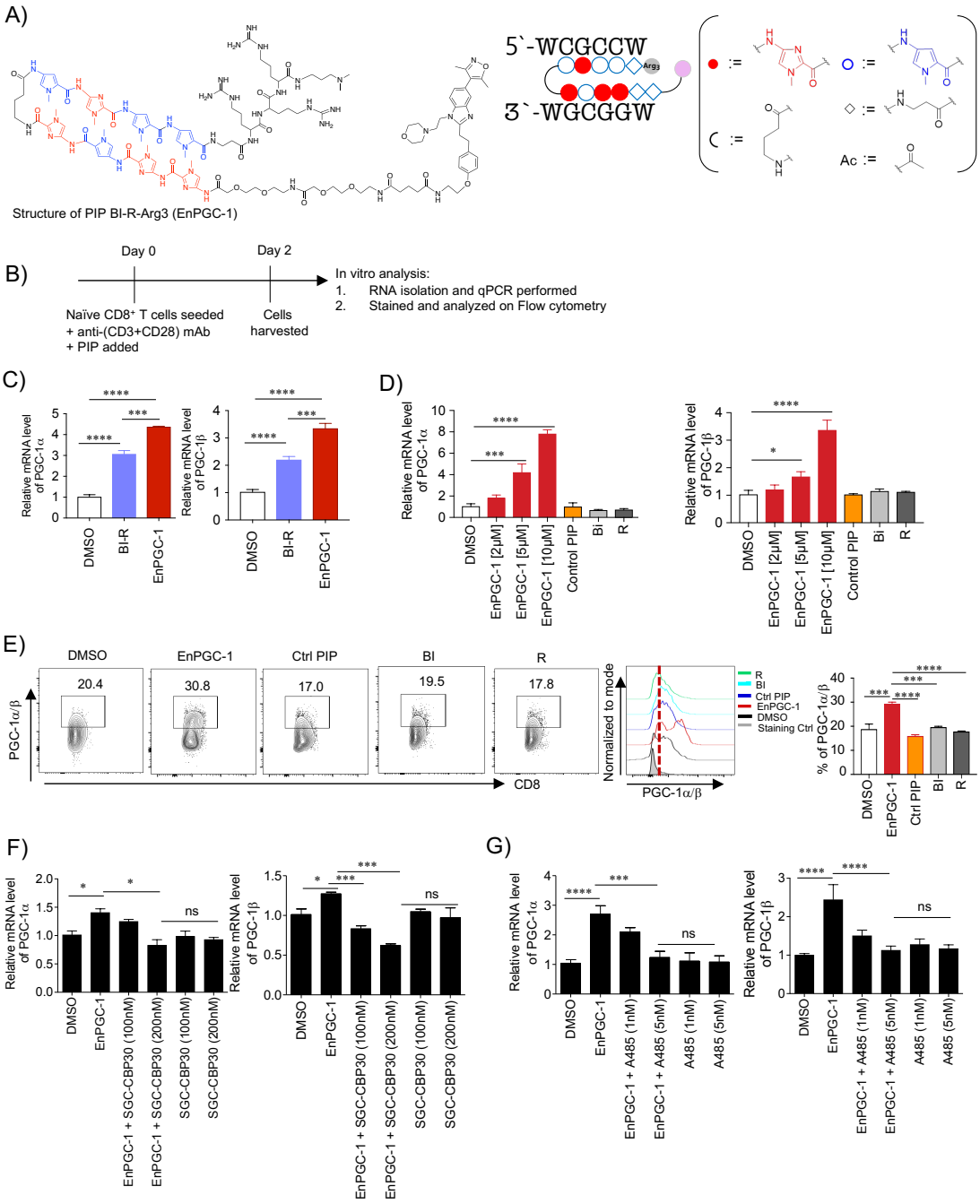
A)
5`-WCGCCW
3`-WGCGGW
Arg3
Ac :=
Structure of PIP BI-R-Arg3 (EnPGC-1)
B)
Day 0
Day 2
Naïve CD8+ T cells seeded
+ anti-(CD3+CD28) mAb
+ PIP added
Cells
harvested
In vitro analysis:
1. RNA isolation and qPCR performed
2. Stained and analyzed on Flow cytometry
C)
Relative mRNA level of PGC-1α
Relative mRNA level of PGC-1β
DMSO
BI-R
EnPGC-1
D)
EnPGC-1 [2μM]
EnPGC-1 [5μM]
EnPGC-1 [10μM]
Control PIP
Bi
R
E)
DMSO
EnPGC-1
Ctrl PIP
BI
R
20.4
30.8
17.0
19.5
17.8
PGC-1α/β
CD8
Normalized to mode
Staining Ctrl
% of PGC-1α/β
F)
EnPGC-1 + SGC-CBP30 (100nM)
EnPGC-1 + SGC-CBP30 (200nM)
SGC-CBP30 (100nM)
SGC-CBP30 (200nM)
ns
G)
EnPGC-1 + A485 (1nM)
EnPGC-1 + A485 (5nM)
A485 (1nM)
A485 (5nM)

1

Figure 2

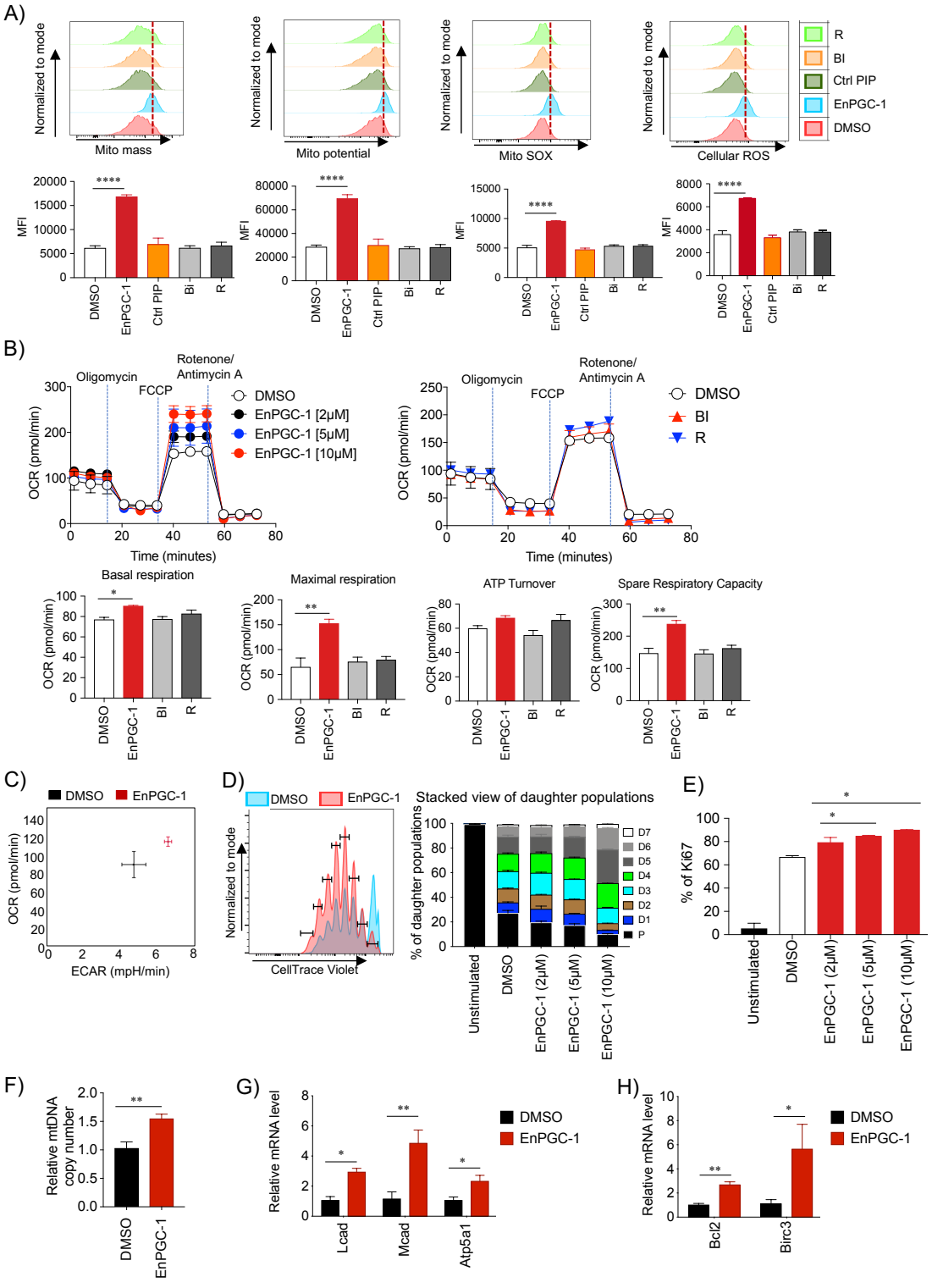
A)
Normalized to mode
Mito mass
Mito potential
Mito SOX
Cellular ROS
R
BI
Ctrl PIP
EnPGC-1
DMSO
MFI
****
DMSO
EnPGC-1
Ctrl PIP
Bi
R
B)
Oligomycin
FCCP
Rotenone/
Antimycin A
OCR (pmol/min)
Time (minutes)
DMSO
EnPGC-1 [2μM]
EnPGC-1 [5μM]
EnPGC-1 [10μM]
BI
R
Basal respiration
Maximal respiration
ATP Turnover
Spare Respiratory Capacity
C)
ECAR (mpH/min)
D)
CellTrace Violet
Stacked view of daughter populations
% of daughter populations
D7
D6
D5
D4
D3
D2
D1
P
Unstimulated
EnPGC-1 (2μM)
EnPGC-1 (5μM)
EnPGC-1 (10μM)
E)
% of Ki67
F)
Relative mtDNA copy number
G)
Relative mRNA level
Lcad
Mcad
Atp5a1
H)
Bcl2
Birc3

1

Figure 3

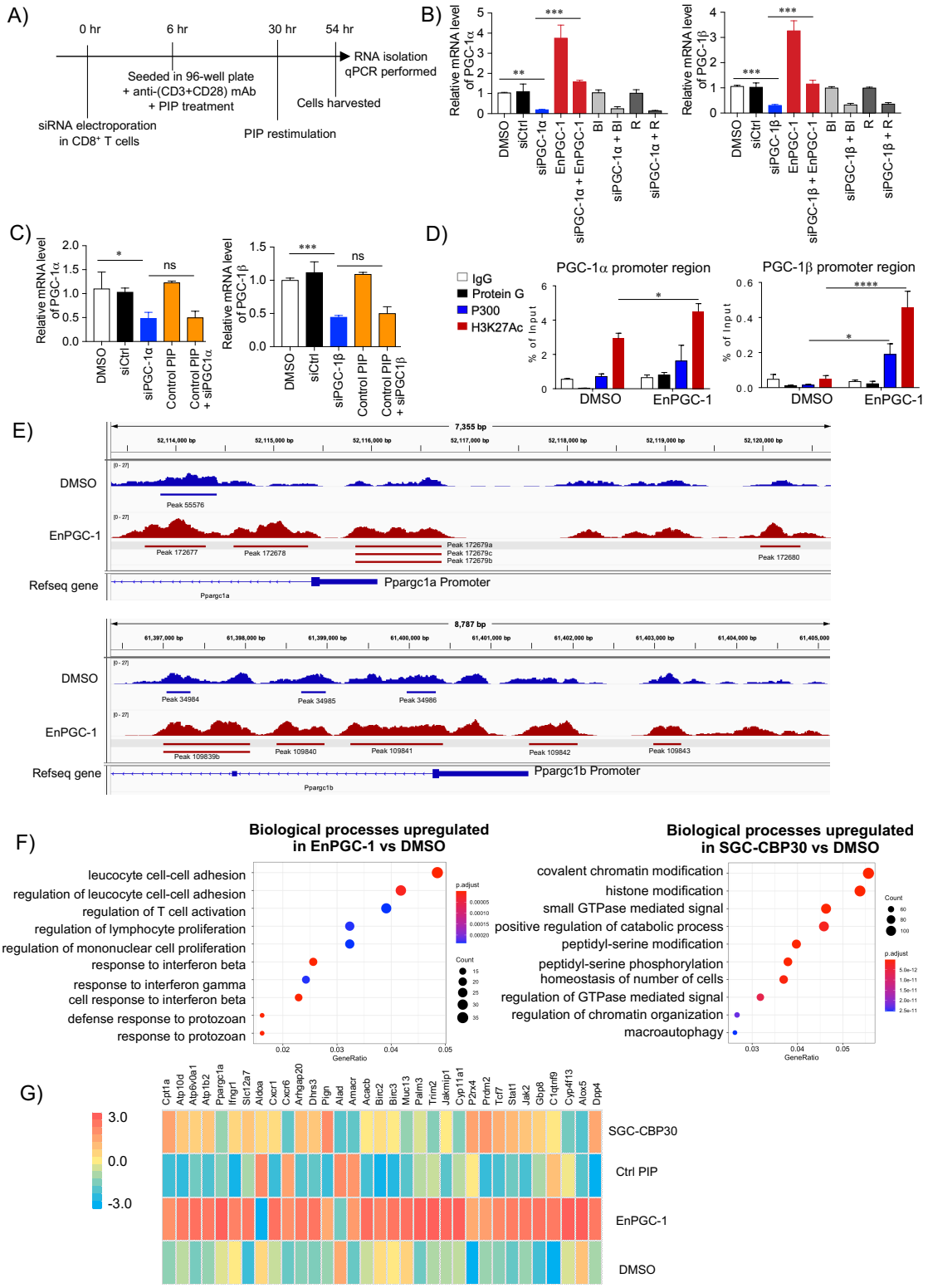
A)
0 hr
6 hr
30 hr
54 hr
RNA isolation
qPCR performed
Seeded in 96-well plate
+ anti-(CD3+CD28) mAb
+ PIP treatment
Cells harvested
siRNA electroporation
in CD8+ T cells
PIP restimulation
B)
Relative mRNA level of PGC-1α
Relative mRNA level of PGC-1β
DMSO
siCtrl
siPGC-1α
siPGC-1β
EnPGC-1
EnPGC-1 + BI
siPGC-1α + BI
siPGC-1β + BI
R
siPGC-1α + R
siPGC-1β + R
C)
Relative mRNA level of PGC-1α
Relative mRNA level of PGC-1β
Control PIP
Control PIP + siPGC1α
Control PIP + siPGC1β
ns
D)
IgG
Protein G
P300
H3K27Ac
PGC-1α promoter region
PGC-1β promoter region
% of Input
DMSO
EnPGC-1
E)
7,355 bp
DMSO
EnPGC-1
Refseq gene
Ppargc1a Promoter
8,787 bp
Ppargc1b Promoter
F)
Biological processes upregulated in EnPGC-1 vs DMSO
leucocyte cell-cell adhesion
regulation of leucocyte cell-cell adhesion
regulation of T cell activation
regulation of lymphocyte proliferation
regulation of mononuclear cell proliferation
response to interferon beta
response to interferon gamma
cell response to interferon beta
defense response to protozoan
response to protozoan
GeneRatio
p.adjust
Count
Biological processes upregulated in SGC-CBP30 vs DMSO
covalent chromatin modification
histone modification
small GTPase mediated signal
positive regulation of catabolic process
peptidyl-serine modification
peptidyl-serine phosphorylation
homeostasis of number of cells
regulation of GTPase mediated signal
regulation of chromatin organization
macroautophagy
G)
SGC-CBP30
Ctrl PIP
EnPGC-1
DMSO

1

Figure 4

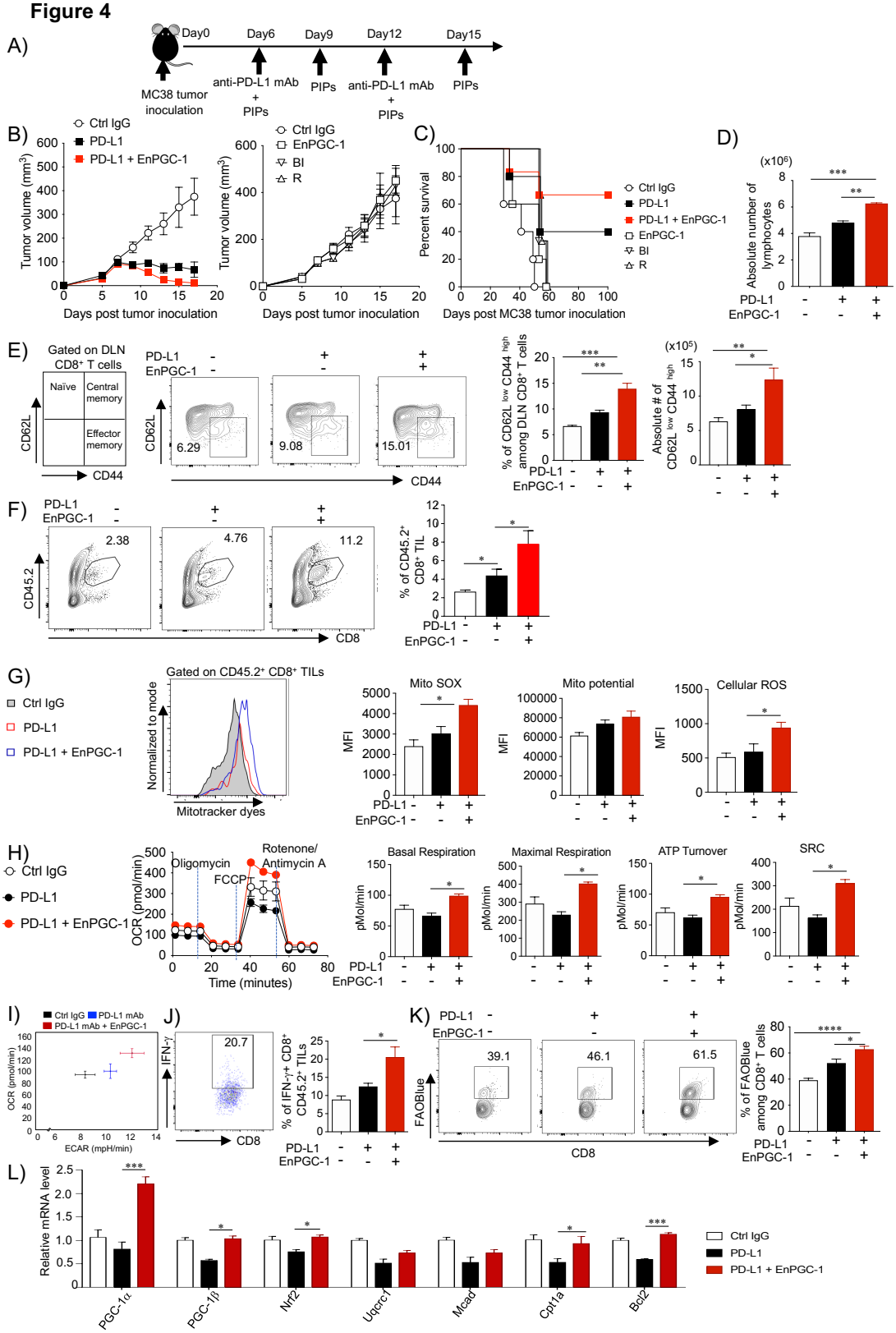
A)
Day0
Day6
Day9
Day12
Day15
MC38 tumor inoculation
anti-PD-L1 mAb + PIPs
PIPs
anti-PD-L1 mAb + PIPs
PIPs
B)
Ctrl IgG
PD-L1
PD-L1 + EnPGC-1
Tumor volume (mm3)
Days post tumor inoculation
Ctrl IgG
EnPGC-1
BI
R
Tumor volume (mm3)
Days post tumor inoculation
C)
Percent survival
Days post MC38 tumor inoculation
Ctrl IgG
PD-L1
PD-L1 + EnPGC-1
EnPGC-1
BI
R
D)
(x10^6)
Absolute number of lymphocytes
PD-L1
EnPGC-1
E)
Gated on DLN CD8+ T cells
Naïve
Central memory
Effector memory
Effector memory
CD62L
CD44
PD-L1
EnPGC-1
6.29
9.08
15.01
% of CD62L low CD44 high among DLN CD8+ T cells
(x10^5)
Absolute # of CD62L low CD44 high
F)
PD-L1
EnPGC-1
2.38
4.76
11.2
CD45.2
CD8
% of CD45.2+ CD8+ TIL
G)
Ctrl IgG
PD-L1
PD-L1 + EnPGC-1
Gated on CD45.2+ CD8+ TILs
Normalized to mode
Mitotracker dyes
Mito SOX
Mito potential
Cellular ROS
MFI
H)
Ctrl IgG
PD-L1
PD-L1 + EnPGC-1
OCR (pmol/min)
Oligomycin
FCCP
Rotenone/ Antimycin A
Time (minutes)
Basal Respiration
Maximal Respiration
ATP Turnover
SRC
pMol/min
I)
Ctrl IgG
PD-L1 mAb
PD-L1 mAb + EnPGC-1
OCR (pmol/min)
ECAR (mpH/min)
J)
IFN-γ
20.7
CD8
% of IFN-γ+ CD8+ CD45.2+ TILs
K)
PD-L1
EnPGC-1
39.1
46.1
61.5
FAOBlue
CD8
% of FAOBlue among CD8+ T cells
L)
Relative mRNA level
PGC-1α
PGC-1β
Nrf2
Uqcrc1
Mcad
Cpt1a
Bcl2
Ctrl IgG
PD-L1
PD-L1 + EnPGC-1

FIGURE LEGENDS

Figure 1. Synthetic sequence-specific epigenetic modulator, EnPGC-1, enhances PGC-1α/β expression

(A) Structural design of EnPGC-1. (B) Schematic representation of experimental schedule for Figure C to G. (C-D) Transcript levels of PGC-1α (left) and PGC-1β (right) in $CD8^+$ T cells treated with 5 μM or indicated conc. of EnPGC-1, BI-R, BI and R. (E) PGC-1α/β protein level was quantified using flow cytometry. Representative FACS pattern (left), histogram (middle) and bar graph showing frequency of PGC-1α/β (right) are shown. (F) Transcript level of PGC-1α (left) or PGC-1β (right) in $CD8^+$ T cells treated with EnPGC-1 and SGC-CBP30 (100 nM and 200 nM). (G) Transcript level of PGC-1α (left) or PGC-1β (right) in $CD8^+$ T cells treated with EnPGC-1 and A485 (1 nM and 5 nM). (C-G) one-way ANOVA analysis. *$p < 0.05$, **$p < 0.01$, ***$p < 0.001$, ****$p < 0.0001$, Means ± SEM, n=3 wells. Data are representative of three independent experiments.

Figure 2. EnPGC-1 enhances mitochondrial activation, proliferation and mitochondrial biogenesis in $CD8^+$ T cells *in vitro*

Following the schedule in Figure 1B, all *in vitro* analyses were performed post 48 h of treatment except D-E where cells were analyzed at 72 h. (A) Mitochondrial activation parameters (mitochondrial mass, potential, mitoSox and cellular ROS) were assessed using mitochondrial dyes. Representative histogram (upper panel) and mean fluorescence intensity (MFI) of different mito dyes (lower panel) are shown. (B) OCR of $CD8^+$ T cells treated with EnPGC-1 (2, 5, 10 μM) and controls (BI and R, each 5 μM conc.) are shown (upper panel). OCR associated parameters were calculated and compared among treated groups (5 μM each) (lower panel). (C) The double plot of OCR/ECAR was plotted (using measurement before oligomycin injection). (D-E) Proliferation was assessed 72 h post stimulation of CellTrace Violet (CTV)- labelled naïve $CD8^+$ T cells treated with EnPGC-1 by dye dilution method (D) or by Ki67 (a proliferation marker) staining method (E). (D) Histogram of dye dilution for DMSO and EnPGC-1 (5 μM) treated is shown (left). The undivided population (high CTV intensity) is the parent population (denoted as P). Different daughter populations (namely D1-D7) were compared in stacked view (right). (E) From the experimental groups of Figure 2D, cells were stained with Ki67 and frequency of Ki67 is shown. (F) mtDNA copy number (mt-ND1/nu-HK2) was assessed in $CD8^+$ T cells. (G-H) Transcript level of different genes were assessed by qRT-PCR from the naïve $CD8^+$ T cells treated with EnPGC-1 (5 μM). (A, B, D, E, G, H) Means ± SEM, n=3 wells, *$p < 0.05$, **$p < 0.01$, ***$p < 0.001$, ****$p < 0.0001$, one-way ANOVA analysis. (F) Means ± SEM, n=3 wells. **$p < 0.01$, two-tailed student t-test analysis. Data are representative of three independent experiments.

Figure 3. EnPGC-1 recruit the acetylation machinery and promote locus-specific acetylation in promoter region and enhance transcription of PGC-α/β

(A) Schematic representation of experimental schedule of siRNA-mediated knockdown assay. (B-C) Transcript level of PGC-1α (left) or PGC-1β (right) in $CD8^+$ T cells from indicated treated groups of siRNA assay. (D) ChIP-PCR of p300 binding and histone H3K27 acetylation in the promoter region of PGC-1α/β in $CD8^+$ T cells treated with EnPGC-1 is shown. The amount of promoter sequence of PGC-1α (left) and PGC-1β (right) in the coprecipitated DNAs was determined by qRT-PCR. (E) ChIP-Seq analysis of H3K27-acetylation in promoter region of Ppargc1a (upper) and Ppargc1b (lower) are shown. (F) RNA-seq of $CD8^+$ T cells treated with PIPs were performed (see material and methods). Biological processes upregulated in EnPGC-1 over DMSO (left), and SGC-CBP30 over DMSO (right) are shown. (G) Heat-map were generated for some particular genes related with OXPHOS, fatty acid metabolism, T cell activation. (B-D) Means ± SEM, n=6 wells, *$p < 0.05$, **$p < 0.01$, ***$p < 0.001$, ****$p < 0.0001$, one-way ANOVA analysis. Data are representative of three independent experiments.

Figure 4. EnPGC-1 synergize with PD-1 blockade therapy and improves the efficacy *in vivo*

(A) Schematic representation of *in vivo* experimental plan. (B-C) Tumor graphs (B) and survival curve (C) were plotted. (D-L) Using the experimental schedule mentioned in Figure 4A, mice were sacrificed one day after third treatment of PIPs (i.e., day 13) and analyzed further. (D) Absolute number of lymphocytes (number of lymphocytes per tDLN) were calculated. (E) Schematic representation of different population of DLN $CD8^+$ T cell subsets is shown based on the expression of CD62L and CD44 (left most). Representative FACS pattern (middle) of effector memory population of tDLN $CD8^+$ T cells were compared among treated groups in both frequency and absolute number (right). (F-G) Tumor mass was harvested, homogenized using collagenase treatment and made single cell suspension for analysis. Tumor mass cells were stained with anti-CD8, anti-CD45.2 mAb along with mitochondrial dyes to assess mitochondrial activation. (F) Representative FACS pattern (left) of $CD8^+$ TILs ($CD45.2^+$ $CD8^+$ T cells) and frequency (right) are shown. (G) Representative histogram of mitochondrial dye (left) and bar graph of MFI of different dyes (right) are shown. (H) Purified $CD8^+$ T cells from pooled DLN cells (of respective groups) were subjected to OCR measurement (see material and methods). OCR graph (left) and OCR associated parameters (right) are shown. (I) Double plot of OCR vs ECAR was plotted (using measurement before oligomycin injection). (J) Representative FACS pattern of IFN-γ staining (left) and frequency of IFN-γ^+CD8^+ TILs (right) are shown. (K) Representative FACS pattern

of FAOBlue staining (left) and their frequency (right) in DLN cells are shown. (L) Transcript level of different genes in DLN $CD8^+$ T cells from *in vivo* experimental groups. (D-H, J-K) Mean ± SEM, n=5 mice. (I, L) Means ± SEM, n=3 wells, *p < 0.05, **p < 0.01, ***p < 0.001, ****p < 0.0001, one-way ANOVA analysis. Data are representative of three independent experiments.

STAR METHODS

RESOURCE AVAILABILITY

Lead contact

Further information and requests for resources and reagents should be directed to and will be fulfilled by the lead contact, Hiroshi Sugiyama (hs@kuchem.kyoto-u.ac.jp).

Materials availability

Compounds generated in this study will be made available upon reasonable request.

Data and code availability

RNA-sequencing and ChIP-sequencing data has been deposited at Gene Expression Omnibus (GEO) repository (http://www.ncbi.nlm.nih.gov/geo). FASTQ files for RNA-seq are available with identification GEO accession number GSE174750 and for ChIP-sequencing are available with identification GSE175849. Data generated in this study will be made available upon reasonable request.

EXPERIMENTAL MODEL AND SUBJECT DETAILS

Cell lines

Cell lines were cultured in DMEM (Gibco, Catalog # 10569-010), RPMI 1640 (Gibco, Catalog # 11875-093) media supplemented with 1% Pen/Strep (nacalai tesck, Catalog # 26253-84) and 10% heat-inactivated fetal bovine serum (FBS) according to the ATCC recommendations. Cell lines were free from mycoplasma contamination and were monitored regularly for contamination. Cell cultures were maintained at 37 C with 5% CO2 in a humidified incubator. Cell cultures were used within four passages for all the experiments in this work. MC38 (murine colorectal carcinoma cell line from C57BL/6N background) cell line was bought from Kerafast Inc, U.S. B16 (murine melanoma cell line from C57BL/6N background) and HDF (human dermal fibroblast) were purchased from ATCC. PIPs were added at the conc. of 5 μM for *in vitro* assays throughout this work wherever it is used unless specified.

Animals and study approval

6-8 weeks old female C57BL/6N mice were purchased from 'CLEA Japan (Tokyo, Japan)' and maintained under specific pathogen-free conditions at the 'Laboratory Animal Research Center, iCeMS, Kyoto University' under the direction of the Institutional Review Board, Kyoto University.

In vivo PD-1 blockade therapy along with PIP

MC38 (0.5 million cells) tumor cells were intradermally (i.d.) injected into the right flank of C57BL/6N mice (day 0). On day 6, combination therapy was started. Anti-PD-L1 mAb (40 μg per mouse, clone 10F.9G2, BioXcell, Catalog# BE0101) and the PIPs EnPGC-1 and other controls (1mg/kg) were injected intraperitoneally (i.p.). PIPs were injected every third day and anti-PD-L1 mAb every sixth days. Therapy was performed up to one month and survival was recorded. Tumor size was measured alternate days using a caliper and tumor volume was calculated using the formula for a typical ellipsoid. For control group, an isotype control for the anti-PD-L1 mAb (Rat IgG2b, k) was injected.

In vivo tumor analysis

Three tumor DLN (tDLN) were harvested and homogenized to make single cell suspension. Absolute number of lymphocytes (number of lymphocytes per DLN) were calculated. DLN cells were stained with anti-CD8, anti-CD62L and anti-CD44 mAbs. $CD8^+$ DLN cells were further extrapolated based on the intensity of CD62L and CD44 and were classified in different $CD8^+$ T cell subsets (naïve, $CD62L^{high}$ $CD44^{low}$; central memory, $CD62L^{high}$ $CD44^{high}$; and effector memory, $CD62L^{low}$ $CD44^{high}$).

METHOD DETAILS

PIP Synthesis

EnPGC-1 was synthesized according to the procedures described previously (Hidaka et al., 2020, Taniguchi et al., 2018). In brief, Fmoc solid-phase synthesis of designed PIP structures was performed on a PSSM-8 (Shimadzu), then cleavage was carried out with 1 ml of 3,3-diamino-N-methyldipropylamine (Dp) for 3 h at 45 °C. The resulting crude PIPs were purified by flash column chromatography. The purified PIPs were then characterized by HPLC and MALDI-TOF/MS. Chemical structure of each PIPs used in this work have been shown with respective HPLC chart and mass spectra in Figure S6.

$CD8^+$ T cell isolation

Naïve $CD8^+$ T ($CD62L^{high}$ $CD44^{low}$) cells were purified from pooled lymphocytes of lymph nodes (axillary, brachial, and inguinal LNs) and spleen from 6-8 weeks old C57BL/6N inbred wild-type female mice. Spleen cells were treated with ACK lysis buffer (0.15 M NH4Cl + 1.0 mM KHCO3 + 0.1 mM Na2-EDTA) for 2 min to lyse the erythrocytes before pooling into lymph node cells. Naïve $CD8^+$ T cells were purified following manufacturer's instructions (Biolegend, Catalog# 480043). For *in vitro* analysis, naïve $CD8^+$ T cells were stimulated with

1 μg/ml conc. of each anti-CD3 mAb (clone 145.2C11, Biolegend, Catalog#100339) and anti-
CD28 mAb (clone 37.51, eBioscience, Catalog#16-0281-85). $CD8^+$ T cells were cultured in
'Spleen RPMI media' (RPMI with 10% FCS, 1% Pen/Strep mix, 1% nonessential amino acids,
50 μM β-mercaptoethanol, 2 mM L-Glutamine, and 1% sodium pyruvate) in all the *in vitro*
experiments throughout this project. Naïve $CD8^+$ T ($CD62L^{high}$ $CD44^{low}$) cells (100 thousand
cell/ well) were seeded in 96-well round bottom plate and stimulated with anti-CD3 and anti-
CD28 mAbs (each 1 μg/mL conc.). PIPs were added 5 μM or indicated conc. and incubated
for 48 h are used for all the downstream analysis.

Flow cytometry analysis

PGC-1α/β protein level quantification

Murine primary $CD8^+$ T cells were given TCR stimulation (with anti-CD3/CD28 mAb)
and treated with EnPGC-1 or other control PIPs as per the schedule mentioned in Figure 1B
and protein level of PGC-1α/β was quantified intranuclearly (Foxp3 staining kit). For staining
PGC-1, the previously reported anti-PGC-1α/β antibody (Abcam, ab72230) was used that
detects both PGC-1α and PGC-1β human/mice (Hatae et al., 2020, Wang et al., 2019).
Isotype control antibodies were used as staining control.

Mitochondrial activation assessment

Mitochondrial activation parameters e.g., potential, mass, and ROS generation were
assessed using vital dyes MitoTracker Deep Red, MitoTracker Green, MitoSOX Red/CellROX
(Life Technologies). The conc. of dyes was used as per recommendation. Cells were incubated
with dyes for 30 minutes followed by wash with PBS and surface staining, if any, e.g., CD45.2
(104, Biolegend), CD44 (IM7, Biolegend), CD8 (53-6.7, Biolegend), CD62L (MEL-14,
Biolegend).

Fatty acid oxidation measurement

FAO was assessed using 'Fatty Acid Oxidation Detection Reagent' (FAOBlue)
(Funakoshi, Catalog#FDV-0033). Cells were first washed twice with D-PBS followed by
addition of FAOBlue (15 μM in serum-free RPMI media) and incubated for 2 h at 37 °C in a
5% CO2 humidified incubator. After incubation, cells were centrifuged, washed twice with
D-PBS and further stained for surface proteins (if any) and analyzed by flow cytometry under
brilliant violet laser.

Cytokine intracellular staining

For intracellular staining, cells were first surface stained (if any) before moving to the
fixation and permeabilization step. After surface staining and washing with FACS buffer (PBS,
0.5-1% BSA or 5-10% FBS, 0.1% NaN3 sodium azide), cells were fixed using
polyparaformaldehyde solution (1.5% in D-PBS; 30 minutes incubation at 4 °C). Cells were

washed using FACS buffer followed by permeabilization using Triton-X solution (0.5% Triton-X-100 in PBS; 30 minutes incubation at 4 °C). Following the incubation, cells were washed with FACS buffer and stained with antibodies against the target protein of interest e.g., Ki67 (clone SolA15, eBioscience), IFN-γ clone XMG-1.2, Biolegend).

Proliferation assay

Naïve $CD8^+$ T cells were isolated and labelled with CellTrace Violet (CTV) (1uM in PBS suspension, 15 minutes, 37 degree,). Staining was quenched with FBS containing media and washed 2 times with FBS containing media. Further, 100 thousand cells were seeded in 96-well round bottom plate and stimulated with anti-CD3/CD28 mAbs (each 1ug/ml). PIPs were added and incubated for 72 h. 72 h post stimulation was considered as good time point to assess proliferation by dye dilution method or by Ki67 (a proliferation marker) staining method.

Squelching assay

Naïve $CD8^+$ T cells were harvested from C57BL/6N mice and TCR stimulated with anti-CD3/anti-CD28 mAbs. In addition, PIP (5 μM) and different doses of SGC-CBP30 (CBP/p300 inhibitor) and A-485 (p300 acetyltransferase inhibitor) were added and stimulated for 48 h. Based on our initial optimization experiments with a range (100 nM-1000 nM) of conc., we chose the working conc. of SGC-CBP30 as 200 nM as a notable cytotoxicity was observed from 500 nM. Likewise, a range of conc. (1-50 nM) were tested for A-485 and we chose to work with 5 nM to clarify the mechanism of inhibition as no notable fold change observed beyond 10 nM.

Real-time RT-PCR

Total RNA was isolated by using RNeasy mini kit (QIAGEN) and generated cDNA by reverse transcription (Invitrogen). 1 μg of total RNA was reverse transcribed into cDNA by ReverTraAce qPCR RTMasterMix with gDNA Remover (Toyobo) and qPCR was performed using THUNDERBIRD SYBR qPCR Mix (Toyobo) in LightCycler 480 (Roche Diagnostics GmbH). 20ng cDNA were run for qPCR analysis. Cp value was determined by the second derivative maximum method and relative RNA amount was calculated. As an internal control, Gapdh was used. The list of the primers used in this work is listed in Table S1.

Mitochondrial DNA copy number assessment

Mitochondrial DNA (mtDNA) copy number was assessed in $CD8^+$ T cells treated with EnPGC-1 (5 μM) or DMSO vehicle. DNA extractions were performed using a QIAamp DNA

mini kit (Qiagen). qPCR was performed to measure the mtDNA copy numbers, using mtDNA-encoded NADH dehydrogenase 1 (ND1) (Refinetti et al., 2017). The abundance of target gene was normalized to the signal for nuclear hexokinase 2 (HK2) gene.

siRNA mediated knockdown assay

Purified $CD8^+$ T cells were electroporated with siRNAs against PGC-1α and PGC-1β using neon electroporation system. The protocol was followed according to manufacturer's instructions for primary T cells. 10 pico mole of siRNA were used per 1 million cells. Electroporated cells were incubated for 6 h in complete nucleofector medium (Amaxa, Catalog# VZB-1001) followed by TCR stimulation (anti-CD3/CD28 mAbs) and PIP (5 μM) treatment. The cells were incubated for 48 h. Following the incubation, cells were harvested, RNA purified, and qPCR was performed (GAPDH was used as loading control). The sequence of siRNA used were as follows: siPGC-1α, CACAACUCCUCCUCAUAAAdTdT; siPGC-1β, CUCAUUCGCUACAUGCAUAdTdT; siCtrl, CAAUACUCUACAAACCCUCdTdT. The siRNA sequences have been listed in Table S1.

T_m analysis

Two DNA oligomers (5'-GGCACGCCTCGG-3' (EnPGC1-DNA), and 5'-GGCAGACGTCGG-3' (Mismatch-DNA)) used in this analysis were purchased from Sigma. The analytical buffer for Tm analysis was aqueous solution of 10 mM sodium chloride and 10 mM Tris-HCl at pH 7.5 containing 0.5% v/v DMSO. The conc. of dsDNA was 2.5 μM. The conc. of polyamides was 5 μM (2 equiv.). Further, samples were annealed from 95 °C to 20 °C (dsDNA with PIP) or 95 °C to 5 °C (DNA only) at 1.0 °C/min. Absorbance at 260 nm was recorded from 20 °C to 95 °C (dsDNA with PIP) or 5 °C to 95 °C (DNA only) at a rate of 1.0° C/min using a spectrophotometer V-650 or V-750 (JASCO) with a thermo-controlled PAC-743R cell changer (JASCO) and a thermal-circulator F25-ED or CTU-100 (JASCO). The Tm values are shown in Figure S3B. The Tm values are the average of technical triplicates and SD were calculated. The template DNA sequences have been listed in Table S1.

Chromatin immunoprecipitation (ChIP) assay

Murine primary $CD8^+$ T cells were TCR stimulated (anti-CD3/anti-CD28 mAb) and treated with PIP (5 μM) for 48 h. ChIP assay for $CD8^+$ T cells was performed using ChIP-IT PBMC kit following manufacturer's protocol (Active Motif, Catalog#53042). For ChIP using B16 cells, 0.5 million cells per 90 mm dish were seeded and next day treated with PIPs for 48

h. Following the treatment, cells were collected, and cross-linking was performed (with 1 % formaldehyde, 10 minutes incubation at RT). 125 mM glycine was then added to stop the reaction. Cells were washed once with PBS and then lysed in Lysis buffer (10 mM Tris-HCl (pH 7.5), 200 mM NaCl, 10 mM EDTA, 1 % (v/v) SDS, supplemented with complete protease inhibitor cocktail (Roche)). The chromatin was then sheared with an ultrasonicator (Covaris, S2). The sheared chromatins were electrophoresed on agarose gel to check the fragment size (Figure S3C). Insoluble precipitates were removed by centrifugation (16000 g, 10 minutes, 4 °C). The sheared chromatin was diluted three times in IP buffer (16.7 mM Tris-HCl, 1.2 mM EDTA, 1.1 % (v/v) TritonX-100, 167 mM NaCl, 0.01 % (v/v) SDS, pH 8.0, supplemented with cOmplete) and precleared with dynabeads protein G (Thermo S20 Fisher Scientific) at 4 °C. To 500 μL of precleared chromatin, 50 μL of protein G dynabeads and 10 μL of the Rabbit pAb isotype control (Abcam, Catalog#ab37415), anti-mouse KAT3B/p300 mAb (Abcam, Catalog# ab54984), anti-mouse H3K27Ac (Abcam, Catalog# ab4729), and anti-mouse histone H4 acetylated (pan-acetyl) (Active motif, Catalog# 39925) were added. Immunoprecipitation was then performed by incubating the mixture for overnight at 4 °C. The beads were then washed once with IP buffer, twice with Wash 1 buffer (20 mM Tris-HCl, 2 mM EDTA, 1.1 % (v/v) TritonX-100, 0.1 % (v/v) SDS, 150 mM NaCl, pH 8.0), twice with Wash 2 buffer (20 mM Tris-HCl, 2 mM EDTA, 1.1 % (v/v) TritonX-100, 0.1 % (v/v) SDS, 500 mM NaCl, pH 8.0), twice with Wash 3 buffer (10 mM Tris-HCl, 1 mM EDTA, 250 mM LiCl, 1 % (v/v) NP-40, 1 % (w/v) sodium deoxycholate, pH 8.0), and twice with TE buffer (10 mM Tris-HCl, 1 mM EDTA, pH 8.0), and then were suspended in 200 μL of Reverse cross-linking buffer (100 mM NaHCO3, 1 % (v/v) SDS). The suspension was supplemented with 1.5 mg/mL of pronase (Sigma Aldrich) and shaken at 42 °C for 2 h, then at 65 °C overnight. For input samples, the precleared chromatin was directly reverse cross-linked without immunoprecipitation. DNA was purified using QIAquick PCR Purification Kit (Qiagen) and quantified by Bioanalyzer (Agilent Technologies) using Agilent High Sensitivity DNA Kit (Agilent Technologies). ChIP products were subjected to PCR-based amplification with the indicated primer sets (see Table S1). ChIP enrichment was calculated as % of Input (ChIP/Input X 100). Enrichment fold in acetylation is calculated by normalizing the data against input DNA and by normalizing the enrichment with IgG antibody. Data represent the means ± SEM of three wells. *$p < 0.05$, **$p < 0.01$, ***$p < 0.001$, one-way ANOVA analysis. Data are representative of two independent experiments. The primers for ChIP-assay have been listed in Table S1.

ChIP-sequencing (ChIP-Seq) analysis

H3K27Ac-ChIP of murine $CD8^+$ T cells treated with EnPGC-1 or DMSO vehicle were

further sequenced to understand the genome-wide acetylation induced by EnPGC-1. ChIP-Sequencing was performed by Macrogen Inc. ChIP-Seq libraries were prepared using TruSeq DNA Sample Prep Kit following the protocol TruSeq ChIP Sample Preparation Guide, Part # 15023092 Rev. B. All libraries were sequenced to a depth of 100 million reads using the NovaSeq6000 sequencer to generate 151-bp paired-end library reads. Following the quality check, Trimmomatic, a fast, multithreaded command line tool was used to trim and crop Illumina (FASTQ) data as well as to remove adapters. Following the read trimming, a guided pipeline was used for the downstream analysis in the sequence e.g., Bowtie (read mapping), Picard (remove duplicates), MACS2 (peak calling) and ChIPseeker (peak annotation). Bowtie tool (version 1.1.2) was used to align short DNA sequences (reads) to the reference mouse genome (mm10). Further, MACS2 (version 2.2.2.20160309) captures the influence of genome complexity to evaluate the significance of enriched ChIP regions, and MACS improves the spatial resolution of binding sites through combining the information of both sequencing tag position and orientation. Duplicate reads were identified by Picard (version 0.118). Further, the final data were annotated using ChIPseeker tool (version v1.16.1). It supports annotating ChIP peaks and provides functions to visualize ChIP peaks coverage over chromosomes and profiles of peaks binding to TSS regions. FASTQ files are available through the Gene Expression Omnibus (GEO) accession number GSE175849.

RNA-Seq data generation

Murine primary $CD8^+$ T cells were TCR stimulated with anti-CD3/CD28 mAb and treated with PIPs for 48 h following the schedule mentioned in Figure 1B. Following the treatment, cells were harvested, and RNA was extracted using the Qiagen RNeasy kit from the treated groups. RNA integrity was assessed using a Bioanalyzer 2100 (Agilent Technologies) and deemed of good quality for conducting the RNA-Sequencing experiment. RNA-Sequencing was performed at Illumina platform by Macrogen Inc. RNA-Seq libraries were prepared using TruSeq Stranded mRNA LT Sample Prep Kit following the protocol TruSeq Stranded mRNA Sample Preparation Guide, Part # 15031047 Rev. E. All libraries were sequenced to a depth of 200 million reads using the NovaSeq6000 sequencer to generate 100-bp paired-end library reads. Mus musculus whole transcriptome sequencing was performed in order to examine the different gene expression profiles. Further, analysis was performed following the RNA-Seq data quality control, including filtering out low-quality reads, separating multiplexed samples by barcode, and removing 3'-adapter sequences, and provided resulting FASTQ files. The data were deposited at Gene Expression Omnibus (GEO) repository (http://www.ncbi.nlm.nih.gov/geo) and the FASTQ files are available through the GEO accession number GSE174750.

RNA-Seq data analysis

To analyze the expression of Mus musculus $CD8^+$ T cells, whole transcriptome, FASTQ files for each sample were mapped to reference genome mm10 with HISAT2. After the read mapping, Stringtie was used for transcript assembly. Expression profile was calculated for each sample and transcript/gene as read count, FPKM (Fragment per Kilobase of transcript per Million mapped reads) and TPM (Transcripts Per Kilobase Million). Performed read counting per gene and used gene count matrix for differential expression analysis with DESeq2. For differential expression analysis, known batches as "-1" and "-2" were included for samples sequenced at two different times using same schedule. Unknown batch variables were predicted with sva package and one variable was identified which was included as well. Gene-enrichment and functional annotation analysis was performed using Gene Ontology (www.gen eontology.org/). The GO gene list have been listed in Table S2.

Measurement of OCR and ECAR using Seahorse XF analyzer

Oxygen consumption rate (OCR) and extracellular acidification rate (ECAR) were measured using an XFe96 Extracellular Flux analyzer (Seahorse Biosciences). Assay medium (OCR medium) was prepared as per recommendation (XF cell Mito Stress Test Kit, Seahorse Bioscience, 103015-100). Electron transport chain modulators e.g., Oligomycin (100 μM), FCCP (100 μM), and Rotenone/Antimycin A (50 μM) were prepared in OCR media and were added 25 μL of suspension in the wells (Oligomycin to well A; FCCP to B; Rotenone/Antimycin A to C and OCR buffer only well D) as per the manufacturer's recommendation. Calibration using calibrant buffer was done before measurement. 0.3 million cells per well were seeded in the XFe96 plate and the OCR/ECAR was measured. After the completion of run, different parameters were calculated from the OCR graph e.g. (a) basal respiration (measurement before oligomycin treatment – nonmitochondrial respiration (b) ATP turnover (measurement before oligomycin - measurement after oligomycin treatment) (c) maximal respiration (measurement after FCCP treatment- non-mitochondrial respiration) (d) spare respiratory capacity is equal to subtraction of basal from maximal. The OCR medium contains glucose (10 mM) so we measured ECAR of the cells in same well as OCR. Basal ECAR should be considered the measurement immediately before oligomycin injection as the OCR media contains optimal glucose level. The double plot of OCR/ECAR for treated groups was plotted with the values of last measurement before oligomycin injection. Glycolytic capacity is the rate after the injection of oligomycin. Basal ECAR subtracted from glycolytic capacity gives the parameter known as glycolytic reserve.

Statistical Analysis

Statistical analysis was performed using Prism 7. The variations of data were evaluated as the means ± standard error of the mean (SEM). Subjects were chosen randomly from the pool with no blinding test for the treatment of subjects. Data represent the means ± SEM of three wells (for all *in vitro* analysis). Data represent the means ± SEM of five mice (In all the flow cytometry assays and measurements from *in vivo* experiment). For analyzing more than two variables, one-way ANOVA analysis followed by Sidak's multiple comparison test was performed while comparing two groups, student t-test was performed. Data were considered as parametric and statistical tests were two-sided where data were considered significant with a p-value <0.05 where the order of significant defined by *p < 0.05, **p < 0.01, ***p < 0.001, ****p < 0.0001. Data are representative of three independent experiments.

REFERENCE

ANGELA, M., ENDO, Y., ASOU, H. K., YAMAMOTO, T., TUMES, D. J., TOKUYAMA, H., YOKOTE, K. & NAKAYAMA, T. 2016. Fatty acid metabolic reprogramming via mTOR-mediated inductions of PPARgamma directs early activation of T cells. *Nat Commun,* 7**,** 13683.

AZIMI, F., SCOLYER, R. A., RUMCHEVA, P., MONCRIEFF, M., MURALI, R., MCCARTHY, S. W., SAW, R. P. & THOMPSON, J. F. 2012. Tumor-infiltrating lymphocyte grade is an independent predictor of sentinel lymph node status and survival in patients with cutaneous melanoma. *J Clin Oncol,* 30**,** 2678-83.

BAI, C., GAO, S., HU, S., LIU, X., LI, H., DONG, J., HUANG, A., ZHU, L., ZHOU, P., LI, S. & SHAO, N. 2020. Self-Assembled Multivalent Aptamer Nanoparticles with Potential CAR-like Characteristics Could Activate T Cells and Inhibit Melanoma Growth. *Molecular Therapy - Oncolytics,* 17**,** 9-20.

BUCK, M. D., O'SULLIVAN, D., KLEIN GELTINK, R. I., CURTIS, J. D., CHANG, C. H., SANIN, D. E., QIU, J., KRETZ, O., BRAAS, D., VAN DER WINDT, G. J., CHEN, Q., HUANG, S. C., O'NEILL, C. M., EDELSON, B. T., PEARCE, E. J., SESAKI, H., HUBER, T. B., RAMBOLD, A. S. & PEARCE, E. L. 2016. Mitochondrial Dynamics Controls T Cell Fate through Metabolic Programming. *Cell,* 166**,** 63-76.

BUCK, M. D., O'SULLIVAN, D. & PEARCE, E. L. 2015. T cell metabolism drives immunity. *J Exp Med,* 212**,** 1345-60.

BUCK, M. D., SOWELL, R. T., KAECH, S. M. & PEARCE, E. L. 2017. Metabolic Instruction of Immunity. *Cell,* 169**,** 570-586.

CHAMOTO, K., CHOWDHURY, P. S., KUMAR, A., SONOMURA, K., MATSUDA, F., FAGARASAN, S. & HONJO, T. 2017. Mitochondrial activation chemicals synergize with surface receptor PD-1 blockade for T cell-dependent antitumor activity. *Proc Natl Acad Sci U S A,* 114**,** E761-E770.

CHAMOTO, K., HATAE, R. & HONJO, T. 2020. Current issues and perspectives in PD-1 blockade cancer immunotherapy. *Int J Clin Oncol*.

CHOI, J. M. & BOTHWELL, A. L. 2012. The nuclear receptor PPARs as important regulators of T-cell functions and autoimmune diseases. *Mol Cells,* 33**,** 217-22.

CHOWDHURY, P. S., CHAMOTO, K., KUMAR, A. & HONJO, T. 2018. PPAR-Induced Fatty Acid Oxidation in T Cells Increases the Number of Tumor-Reactive CD8(+) T Cells and Facilitates Anti-PD-1 Therapy. *Cancer Immunol Res,* 6**,** 1375-1387.

COUZIN-FRANKEL, J. 2013. Breakthrough of the year 2013. Cancer immunotherapy. *Science,* 342**,** 1432-3.

DANCY, B. M., CRUMP, N. T., PETERSON, D. J., MUKHERJEE, C., BOWERS, E. M., AHN, Y.-H., YOSHIDA, M., ZHANG, J., MAHADEVAN, L. C., MEYERS, D. J., BOEKE, J. D. & COLE, P. A. 2012. Live-Cell Studies of p300/CBP Histone Acetyltransferase Activity and Inhibition. *ChemBioChem,* 13**,** 2113-2121.

DERVAN, P. B. & EDELSON, B. S. 2003. Recognition of the DNA minor groove by pyrrole-imidazole polyamides. *Curr Opin Struct Biol,* 13**,** 284-99.

DUNN, G. P., OLD, L. J. & SCHREIBER, R. D. 2004. The immunobiology of cancer immunosurveillance and immunoediting. *Immunity,* 21**,** 137-48.

FIFE, B. T. & BLUESTONE, J. A. 2008. Control of peripheral T-cell tolerance and autoimmunity via the CTLA-4 and PD-1 pathways. *Immunol Rev,* 224**,** 166-82.

FUKASAWA, A., AOYAMA, T., NAGASHIMA, T., FUKUDA, N., UENO, T., SUGIYAMA, H., NAGASE, H. & MATSUMOTO, Y. 2009. Pharmacokinetics of pyrrole-imidazole polyamides after intravenous administration in rat. *Biopharm Drug Dispos,* 30**,** 81-9.

GALLAGHER, S. J., SHKLOVSKAYA, E. & HERSEY, P. 2017. Epigenetic modulation in cancer immunotherapy. *Curr Opin Pharmacol,* 35**,** 48-56.

HAN, L., PANDIAN, G. N., CHANDRAN, A., SATO, S., TANIGUCHI, J., KASHIWAZAKI, G., SAWATANI, Y., HASHIYA, K., BANDO, T., XU, Y., QIAN, X. & SUGIYAMA, H. 2015. A Synthetic DNA-Binding Domain Guides Distinct Chromatin-Modifying Small Molecules to Activate an Identical Gene Network. *Angewandte Chemie International Edition,* 54**,** 8700-8703.

HATAE, R., CHAMOTO, K., KIM, Y. H., SONOMURA, K., TANEISHI, K., KAWAGUCHI, S., YOSHIDA, H., OZASA, H., SAKAMORI, Y., AKRAMI, M., FAGARASAN, S.,

MASUDA, I., OKUNO, Y., MATSUDA, F., HIRAI, T. & HONJO, T. 2020. Combination of host immune metabolic biomarkers for the PD-1 blockade cancer immunotherapy. *JCI Insight,* 5.

HIDAKA, T., TSUBONO, Y., HASHIYA, K., BANDO, T., PANDIAN, G. N. & SUGIYAMA, H. 2020. Enhanced nuclear accumulation of pyrrole–imidazole polyamides by incorporation of the tri-arginine vector. *Chemical Communications*.

HIRAOKA, K., INOUE, T., TAYLOR, R. D., WATANABE, T., KOSHIKAWA, N., YODA, H., SHINOHARA, K.-I., TAKATORI, A., SUGIMOTO, H., MARU, Y., DENDA, T., FUJIWARA, K., BALMAIN, A., OZAKI, T., BANDO, T., SUGIYAMA, H. & NAGASE, H. 2015. Inhibition of KRAS codon 12 mutants using a novel DNA-alkylating pyrrole–imidazole polyamide conjugate. *Nature Communications,* 6**,** 6706.

IDOS, G. E., KWOK, J., BONTHALA, N., KYSH, L., GRUBER, S. B. & QU, C. 2020. The Prognostic Implications of Tumor Infiltrating Lymphocytes in Colorectal Cancer: A Systematic Review and Meta-Analysis. *Scientific Reports,* 10**,** 3360.

INOKI, K., KIM, J. & GUAN, K. L. 2012. AMPK and mTOR in cellular energy homeostasis and drug targets. *Annu Rev Pharmacol Toxicol,* 52**,** 381-400.

IWAI, Y., ISHIDA, M., TANAKA, Y., OKAZAKI, T., HONJO, T. & MINATO, N. 2002. Involvement of PD-L1 on tumor cells in the escape from host immune system and tumor immunotherapy by PD-L1 blockade. *Proc Natl Acad Sci U S A,* 99**,** 12293-7.

JUNEJA, V. R., MCGUIRE, K. A., MANGUSO, R. T., LAFLEUR, M. W., COLLINS, N., HAINING, W. N., FREEMAN, G. J. & SHARPE, A. H. 2017. PD-L1 on tumor cells is sufficient for immune evasion in immunogenic tumors and inhibits CD8 T cell cytotoxicity. *Journal of Experimental Medicine,* 214**,** 895-904.

KOBAYASHI, H., HATAKEYAMA, H., NISHIMURA, H., YOKOTA, M., SUZUKI, S., TOMABECHI, Y., SHIROUZU, M., OSADA, H., MIMAKI, M., GOTO, Y.-I. & YOSHIDA, M. 2021. Chemical reversal of abnormalities in cells carrying mitochondrial DNA mutations. *Nature Chemical Biology,* 17**,** 335-343.

KRESSLER, D., SCHREIBER, S. N., KNUTTI, D. & KRALLI, A. 2002. The PGC-1-related protein PERC is a selective coactivator of estrogen receptor alpha. *J Biol Chem,* 277**,** 13918-25.

KUMAR, A. & CHAMOTO, K. 2021. Immune metabolism in PD-1 blockade-based cancer immunotherapy. *International Immunology,* 33**,** 17-26.

KUMAR, A., CHAMOTO, K., CHOWDHURY, P. S. & HONJO, T. 2020. Tumors attenuating the mitochondrial activity in T cells escape from PD-1 blockade therapy. *Elife,* 9. Elife. 2020 Mar 3;9:e52330. doi: 10.7554/eLife.52330

LEACH, D. R., KRUMMEL, M. F. & ALLISON, J. P. 1996. Enhancement of antitumor immunity by CTLA-4 blockade. *Science,* 271**,** 1734-6.

LIN, J., HANDSCHIN, C. & SPIEGELMAN, B. M. 2005. Metabolic control through the PGC-1 family of transcription coactivators. *Cell Metab,* 1**,** 361-70.

LIN, J., PUIGSERVER, P., DONOVAN, J., TARR, P. & SPIEGELMAN, B. M. 2002. Peroxisome proliferator-activated receptor gamma coactivator 1beta (PGC-1beta), a novel PGC-1-related transcription coactivator associated with host cell factor. *J Biol Chem,* 277**,** 1645-8.

MAHMOUD, S. M., PAISH, E. C., POWE, D. G., MACMILLAN, R. D., GRAINGE, M. J., LEE, A. H., ELLIS, I. O. & GREEN, A. R. 2011. Tumor-infiltrating CD8+ lymphocytes predict clinical outcome in breast cancer. *J Clin Oncol,* 29**,** 1949-55.

MALINEE, M., KUMAR, A., HIDAKA, T., HORIE, M., HASEGAWA, K., PANDIAN, G. N. & SUGIYAMA, H. 2020. Targeted suppression of metastasis regulatory transcription factor SOX2 in various cancer cell lines using a sequence-specific designer pyrrole-imidazole polyamide. *Bioorg Med Chem,* 28**,** 115248.

MENK, A. V., SCHARPING, N. E., MORECI, R. S., ZENG, X., GUY, C., SALVATORE, S., BAE, H., XIE, J., YOUNG, H. A., WENDELL, S. G. & DELGOFFE, G. M. 2018. Early TCR Signaling Induces Rapid Aerobic Glycolysis Enabling Distinct Acute T Cell Effector Functions. *Cell Rep,* 22**,** 1509-1521.

ODORIZZI, P. M., PAUKEN, K. E., PALEY, M. A., SHARPE, A. & WHERRY, E. J. 2015. Genetic absence of PD-1 promotes accumulation of terminally differentiated exhausted CD8+ T cells. *J Exp Med,* 212**,** 1125-37.

PANDIAN, G. N., SATO, S., ANANDHAKUMAR, C., TANIGUCHI, J., TAKASHIMA, K., SYED, J., HAN, L., SAHA, A., BANDO, T., NAGASE, H. & SUGIYAMA, H. 2014a. Identification of a Small Molecule That Turns ON the Pluripotency Gene Circuitry in Human Fibroblasts. *ACS Chemical Biology,* 9**,** 2729-2736.

PANDIAN, G. N., TANIGUCHI, J., JUNETHA, S., SATO, S., HAN, L., SAHA, A., ANANDHAKUMAR, C., BANDO, T., NAGASE, H., VAIJAYANTHI, T., TAYLOR, R. D. & SUGIYAMA, H. 2014b. Distinct DNA-based epigenetic switches trigger transcriptional activation of silent genes in human dermal fibroblasts. *Scientific Reports,* 4**,** 3843.

PATSOUKIS, N., BARDHAN, K., CHATTERJEE, P., SARI, D., LIU, B., BELL, L. N., KAROLY, E. D., FREEMAN, G. J., PETKOVA, V., SETH, P., LI, L. & BOUSSIOTIS, V. A. 2015. PD-1 alters T-cell metabolic reprogramming by inhibiting glycolysis and promoting lipolysis and fatty acid oxidation. *Nat Commun,* 6**,** 6692.

PAUMEN, M. B., ISHIDA, Y., HAN, H., MURAMATSU, M., EGUCHI, Y., TSUJIMOTO, Y. & HONJO, T. 1997. Direct interaction of the mitochondrial membrane protein carnitine palmitoyltransferase I with Bcl-2. *Biochem Biophys Res Commun,* 231**,** 523-5.

PEARCE, E. L. 2010. Metabolism in T cell activation and differentiation. *Current opinion in immunology,* 22**,** 314-320.

PEARCE, E. L., WALSH, M. C., CEJAS, P. J., HARMS, G. M., SHEN, H., WANG, L.-S., JONES, R. G. & CHOI, Y. 2009. Enhancing CD8 T-cell memory by modulating fatty acid metabolism. *Nature,* 460**,** 103-107.

PERIANAYAGAM, M. C., MADIAS, N. E., PEREIRA, B. J. & JABER, B. L. 2006. CREB transcription factor modulates Bcl2 transcription in response to C5a in HL-60-derived neutrophils. *Eur J Clin Invest,* 36**,** 353-61.

PICCA, A. & LEZZA, A. M. 2015. Regulation of mitochondrial biogenesis through TFAM-mitochondrial DNA interactions: Useful insights from aging and calorie restriction studies. *Mitochondrion,* 25**,** 67-75.

PUIGSERVER, P., WU, Z., PARK, C. W., GRAVES, R., WRIGHT, M. & SPIEGELMAN, B. M. 1998. A cold-inducible coactivator of nuclear receptors linked to adaptive thermogenesis. *Cell,* 92**,** 829-39.

REFINETTI, P., WARREN, D., MORGENTHALER, S. & EKSTRØM, P. O. 2017. Quantifying mitochondrial DNA copy number using robust regression to interpret real time PCR results. *BMC Research Notes,* 10**,** 593.

SCHARPING, N. E., MENK, A. V., MORECI, R. S., WHETSTONE, R. D., DADEY, R. E., WATKINS, S. C., FERRIS, R. L. & DELGOFFE, G. M. 2016. The Tumor Microenvironment Represses T Cell Mitochondrial Biogenesis to Drive Intratumoral T Cell Metabolic Insufficiency and Dysfunction. *Immunity,* 45**,** 701-703.

SCHRODER, K., HERTZOG, P. J., RAVASI, T. & HUME, D. A. 2004. Interferon-gamma: an overview of signals, mechanisms and functions. *J Leukoc Biol,* 75**,** 163-89.

SENA, L. A., LI, S., JAIRAMAN, A., PRAKRIYA, M., EZPONDA, T., HILDEMAN, D. A., WANG, C. R., SCHUMACKER, P. T., LICHT, J. D., PERLMAN, H., BRYCE, P. J. & CHANDEL, N. S. 2013. Mitochondria are required for antigen-specific T cell activation through reactive oxygen species signaling. *Immunity,* 38**,** 225-36.

SHAO, S., XU, Q., YU, X., PAN, R. & CHEN, Y. 2020. Dipeptidyl peptidase 4 inhibitors and their potential immune modulatory functions. *Pharmacol Ther,* 209**,** 107503.

ST-PIERRE, J., LIN, J., KRAUSS, S., TARR, P. T., YANG, R., NEWGARD, C. B. & SPIEGELMAN, B. M. 2003. Bioenergetic analysis of peroxisome proliferator-

activated receptor gamma coactivators 1alpha and 1beta (PGC-1alpha and PGC-1beta) in muscle cells. *J Biol Chem,* 278**,** 26597-603.

SYNOLD, T. W., XI, B., WU, J., YEN, Y., LI, B. C., YANG, F., PHILLIPS, J. W., NICKOLS, N. G. & DERVAN, P. B. 2012. Single-dose pharmacokinetic and toxicity analysis of pyrrole-imidazole polyamides in mice. *Cancer chemotherapy and pharmacology,* 70**,** 617-625.

TAKAHASHI, T., ASAMI, Y., KITAMURA, E., SUZUKI, T., WANG, X., IGARASHI, J., MOROHASHI, A., SHINOJIMA, Y., KANOU, H., SAITO, K., TAKASU, T., NAGASE, H., HARADA, Y., KURODA, K., WATANABE, T., KUMAMOTO, S., AOYAMA, T., MATSUMOTO, Y., BANDO, T., SUGIYAMA, H., YOSHIDA-NORO, C., FUKUDA, N. & HAYASHI, N. 2008. Development of pyrrole-imidazole polyamide for specific regulation of human aurora kinase-A and -B gene expression. *Chem Biol,* 15**,** 829-41.

TANIGUCHI, J., FENG, Y., PANDIAN, G. N., HASHIYA, F., HIDAKA, T., HASHIYA, K., PARK, S., BANDO, T., ITO, S. & SUGIYAMA, H. 2018. Biomimetic Artificial Epigenetic Code for Targeted Acetylation of Histones. *Journal of the American Chemical Society,* 140**,** 7108-7115.

TOPALIAN, S. L., DRAKE, C. G. & PARDOLL, D. M. 2015. Immune checkpoint blockade: a common denominator approach to cancer therapy. *Cancer Cell,* 27**,** 450-61.

TUMEH, P. C., HARVIEW, C. L., YEARLEY, J. H., SHINTAKU, I. P., TAYLOR, E. J., ROBERT, L., CHMIELOWSKI, B., SPASIC, M., HENRY, G., CIOBANU, V., WEST, A. N., CARMONA, M., KIVORK, C., SEJA, E., CHERRY, G., GUTIERREZ, A. J., GROGAN, T. R., MATEUS, C., TOMASIC, G., GLASPY, J. A., EMERSON, R. O., ROBINS, H., PIERCE, R. H., ELASHOFF, D. A., ROBERT, C. & RIBAS, A. 2014. PD-1 blockade induces responses by inhibiting adaptive immune resistance. *Nature,* 515**,** 568-71.

TURNER, B. M. 1991. Histone acetylation and control of gene expression. *J Cell Sci,* 99 (Pt 1)**,** 13-20.

VAIJAYANTHI, T., BANDO, T., PANDIAN, G. N. & SUGIYAMA, H. 2012. Progress and Prospects of Pyrrole-Imidazole Polyamide–Fluorophore Conjugates as Sequence-Selective DNA Probes. *ChemBioChem,* 13**,** 2170-2185.

VAN DER WINDT, G. J., EVERTS, B., CHANG, C. H., CURTIS, J. D., FREITAS, T. C., AMIEL, E., PEARCE, E. J. & PEARCE, E. L. 2012. Mitochondrial respiratory capacity is a critical regulator of CD8+ T cell memory development. *Immunity,* 36**,** 68-78.

VAN DER WINDT, G. J., O'SULLIVAN, D., EVERTS, B., HUANG, S. C., BUCK, M. D., CURTIS, J. D., CHANG, C. H., SMITH, A. M., AI, T., FAUBERT, B., JONES, R. G., PEARCE, E. J. & PEARCE, E. L. 2013. CD8 memory T cells have a bioenergetic advantage that underlies their rapid recall ability. *Proc Natl Acad Sci U S A,* 110**,** 14336-41.

VAN DER WINDT, G. J. & PEARCE, E. L. 2012. Metabolic switching and fuel choice during T-cell differentiation and memory development. *Immunol Rev,* 249**,** 27-42.

VERDONE, L., AGRICOLA, E., CASERTA, M. & DI MAURO, E. 2006. Histone acetylation in gene regulation. *Briefings in Functional Genomics,* 5**,** 209-221.

VILLENA, J. A. & KRALLI, A. 2008. ERRalpha: a metabolic function for the oldest orphan. *Trends Endocrinol Metab,* 19**,** 269-76.

WAN, H., XU, B., ZHU, N. & REN, B. 2020. PGC-1 α activator-induced fatty acid oxidation in tumor-infiltrating CTLs enhances effects of PD-1 blockade therapy in lung cancer. *Tumori,* 106**,** 55-63.

WANG, Y., AN, H., LIU, T., QIN, C., SESAKI, H., GUO, S., RADOVICK, S., HUSSAIN, M., MAHESHWARI, A., WONDISFORD, F. E., O'ROURKE, B. & HE, L. 2019. Metformin Improves Mitochondrial Respiratory Activity through Activation of AMPK. *Cell Rep,* 29**,** 1511-1523.e5.

WEINBERG, S. E., SENA, L. A. & CHANDEL, N. S. 2015. Mitochondria in the regulation of innate and adaptive immunity. *Immunity,* 42**,** 406-17.

XU, J., JI, J. & YAN, X. H. 2012. Cross-talk between AMPK and mTOR in regulating energy balance. *Crit Rev Food Sci Nutr,* 52**,** 373-81.

ZHU, H., BENGSCH, F., SVORONOS, N., RUTKOWSKI, M. R., BITLER, B. G., ALLEGREZZA, M. J., YOKOYAMA, Y., KOSSENKOV, A. V., BRADNER, J. E., CONEJO-GARCIA, J. R. & ZHANG, R. 2016. BET Bromodomain Inhibition Promotes Anti-tumor Immunity by Suppressing PD-L1 Expression. *Cell Rep,* 16**,** 2829-2837.

ZOU, W., WOLCHOK, J. D. & CHEN, L. 2016. PD-L1 (B7-H1) and PD-1 pathway blockade for cancer therapy: Mechanisms, response biomarkers, and combinations. *Sci Transl Med,* 8**,** 328rv4.

ZUCCONI, B. E., LUEF, B., XU, W., HENRY, R. A., NODELMAN, I. M., BOWMAN, G. D., ANDREWS, A. J. & COLE, P. A. 2016. Modulation of p300/CBP Acetylation of Nucleosomes by Bromodomain Ligand I-CBP112. *Biochemistry,* 55**,** 3727-34.